

Improving CP Measurement with THEIA and Muon Decay at Rest

Shao-Feng Ge,^{1,2,*} Chui-Fan Kong,^{1,2,†} and Pedro Pasquini^{1,2,‡}

¹*Tsung-Dao Lee Institute & School of Physics and Astronomy,
Shanghai Jiao Tong University, Shanghai 200240, China*

²*Key Laboratory for Particle Astrophysics and Cosmology (MOE)
& Shanghai Key Laboratory for Particle Physics and Cosmology,
Shanghai Jiao Tong University, Shanghai 200240, China*

We explore the possibility of using the recently proposed THEIA detector to measure the $\bar{\nu}_\mu \rightarrow \bar{\nu}_e$ oscillation with neutrinos from a muon decay at rest (μ DAR) source to improve the leptonic CP phase measurement. Due to its intrinsic low-energy beam, this μ THEIA configuration (μ DAR neutrinos at THEIA) is only sensitive to the genuine leptonic CP phase δ_D and not contaminated by the matter effect. With detailed study of neutrino energy reconstruction and backgrounds at the THEIA detector, we find that the combination with the high-energy DUNE can significantly reduce the CP uncertainty, especially around the maximal CP violation cases $\delta_D = \pm 90^\circ$. Both the μ THEIA-25 with 17kt and μ THEIA-100 with 70 kt fiducial volumes are considered. For DUNE + μ THEIA-100, the CP uncertainty can be better than 8° .

I. INTRODUCTION

The charge-parity (CP) symmetry violation is a key to understand the existence of baryon asymmetry in the Universe, namely, why there are more matter than anti-matter [1–5]. There are at least two possible sources of CP violation in the Standard Model (SM) of particle physics: the CP phase in the quark mixing matrix [6, 7] and the leptonic CP phases in the neutrino mixing matrix [8]. Especially, the leptonic CP phases at low energy play an important role [9, 10] in the leptogenesis mechanism [11–13]. Both the Dirac and Majorana CP phases can contribute to the leptogenesis mechanism. However, only the Dirac CP phase manifests itself in neutrino oscillation and can be measured by oscillation experiments [14].

The nonzero reactor mixing angle ($\theta_r \equiv \theta_{13}$) measured by Daya Bay [15] and RENO [16] heralds the precision era of neutrino oscillation experiments. A nonzero θ_r allows the Dirac CP phase δ_D to have physical effect since these two variables always appear together as $\sin \theta_r e^{\pm i\delta_D}$ in the standard parametrization [8] of the Pontecorvo-Maki-Nakagawa-Sakata (PMNS) matrix [17, 18]. Typically, the neutrino oscillations from the muon flavor to the electron flavor ($\nu_\mu \rightarrow \nu_e$ and $\bar{\nu}_\mu \rightarrow \bar{\nu}_e$) are used by the long-baseline accelerator experiments to measure δ_D [19].

The current long-baseline experiments T2K [20] and NO ν A [21] are approaching the discovery threshold. The 2019 T2K result [22] with $\delta_D = 252^\circ_{-33^\circ}^{+40^\circ}$ and $281^\circ_{-31^\circ}^{+28^\circ}$ for the normal and inverted orderings (NO and IO), respectively, has excluded almost half of the parameter space except $[165^\circ, 358^\circ]$ and $[-214^\circ, 342^\circ]$ at 3σ confidence level (C.L.). It is interesting to see that the maximal CP phase $\delta_D = -90^\circ$ is around the best-fit point. However, the 2019 NO ν A result is $\delta_D = 0^\circ_{-23^\circ}^{+74^\circ}$

[23] for NO with best-fit value at vanishing CP phase, $\delta_D = 0^\circ$. In 2021, T2K and NO ν A updated their results with the best-fit value from T2K remaining the same, $\delta_D = 252^\circ_{-33^\circ}^{+40^\circ}$ (NO) and $281^\circ_{-31^\circ}^{+28^\circ}$ (IO) [24] while the NO ν A best fit changes to $\delta_D = 148^\circ_{-157^\circ}^{+49^\circ}$ for NO [25].

Although not significant, there is a tension between the T2K and NO ν A data that they exclude each other at 1σ C.L. [26, 27]. New physics can explain the tension. Both belonging to accelerator neutrino experiments, T2K and NO ν A have very different configurations. While the T2K baseline is 295 km and the peak energy is at 0.6 GeV, the NO ν A baseline is 810 km and peak energy at 2 GeV. These differences in baseline and beam energy leave room for new physics. For example, the non-standard interaction (NSI) contributes extra matter potential [28] and hence its effect on oscillation probabilities is energy dependent [29, 30] to provide a possible solution [31, 32]. The tension is reduced when the data are analyzed in the context of Lorentz invariance violation (LIV). However, it is accompanied by a new mild tension between the best-fit values of $\sin^2 \theta_{23}$ [33]. Besides, the non-unitarity mixing due to heavy neutrinos [34–36] allows extra CP phases to fake the genuine CP effect which can also explain the tension [37]. However, a more recent work [38] points out the non-unitarity cannot explain the tension with the bounds on non-unitarity parameters from the combination of short- and long-baseline data. Similar thing happens for the light sterile neutrino scheme [39]. Whether this tension is truly new physics or not needs further investigation at current and future experiments.

Even if the current tension between T2K and NO ν A measurements vanishes with more data, correct interpretation of CP measurements still faces intrinsic issues including event rate inefficiency, $\delta_D \leftrightarrow \pi - \delta_D$ degeneracy, and large CP uncertainty around the maximal values [40–42]. These issues still remain for the next-generation experiments like T2HK [43] and DUNE [44]. Although its wide spectrum can help to reduce the δ_D degeneracy, DUNE has much larger matter effect than T2K and

* gesf@sjtu.edu.cn

† kongcf@sjtu.edu.cn

‡ ppasquini@sjtu.edu.cn

NO ν A due to higher energy peaking around 2.5 GeV [45]. At long-baseline experiments, the genuine CP effect can be faked by the ubiquitous matter effect, reducing the experimental sensitivity to δ_D [46–48]. In addition, the uncertainties in the matter effect can also reduce the CP sensitivity at DUNE [45].

In this paper, we propose μ THEIA as combination of the THEIA detector [49–52] and a μ DAR neutrino flux to improve the Dirac leptonic CP phase measurement together with DUNE. Sec. II summarizes the contamination of matter effect in the CP measurement and explains why the μ DAR neutrino flux with lower energy can help. Then in Sec. III, we describe the low-energy mode at μ THEIA and the high-energy mode at DUNE, including selection criteria, energy reconstruction, smearing, and backgrounds. A combination of μ THEIA and DUNE can significantly improve the CP sensitivity as illustrated in Sec. IV. Therein, we also give the details of simulation and χ^2 analysis. Our μ THEIA proposal is compared with the existing configurations/proposals in Sec. IV D and summarized in Sec. V.

II. IMPROVING CP MEASUREMENT WITH MULTIPLE BASELINES AND BEAM ENERGIES

The current T2K and NO ν A experiment aims for the discovery of leptonic CP violation, namely, excluding $\delta_D = 0$ and π . Once a nontrivial δ_D is measured, the next step is precision measurement of its value. Several experimental configurations have been proposed to improve the CP measurement after the reactor mixing angle θ_r was measured by Daya Bay and RENO. The upgrade from existing experiments includes: (1) Intensity Upgrade: the beam intensity is significantly enhanced, such as T2K-II [53]; (2) Detector Upgrade: T2HK [43] has a much larger detector Hyper-K than Super-K; (3) Spectrum Upgrade: DUNE [44] adopts wider on-axis spectrum than the off-axis one of NO ν A; and (4) Baseline Upgrade with longer baseline such as T2HKK [54–56] and DUNE. In addition, there are also several new proposals: (5) the accelerator experiments such as P2O [57], ESS ν SB [58], and MOMENT [59]; (6) CP measurement with sub-GeV atmospheric neutrino oscillation such as Super-PINGU [60, 61], Super-ORCA [62], and even at JUNO [63] or DUNE [64]. Comparison among various experimental configurations can be found in [65–68].

A. Matter Contamination on CP Measurement

However, the neutrino energy for all these designs is not low enough to avoid contamination from the ubiquitous matter effect [45, 69–74]. We will try to describe how the CP measurement is contaminated by the matter effect. Based on this, one can see the possible solutions.

The neutrino propagation through matter is described

by the following Hamiltonian [28, 75],

$$\mathcal{H}_M = \frac{1}{2E_\nu} U \begin{pmatrix} 0 & 0 & 0 \\ 0 & \Delta m_s^2 & 0 \\ 0 & 0 & \Delta m_a^2 \end{pmatrix} U^\dagger + \begin{pmatrix} V & 0 & 0 \\ 0 & 0 & 0 \\ 0 & 0 & 0 \end{pmatrix}. \quad (1)$$

The first term is the vacuum Hamiltonian that is a product of the PMNS matrix U [17, 18] and the diagonal mass matrix with solar $\Delta m_s^2 \equiv \Delta m_{21}^2$ and atmospheric $\Delta m_a^2 \equiv \Delta m_{31}^2$ mass squared differences. The neutrino energy E_ν in the denominator contributes as an overall factor. So it is not a suppression in the vacuum term but actually an enhancement of the matter potential in the second term.

Induced by the SM weak interaction, the matter potential $V \equiv \sqrt{2}G_F n_e$ is proportional to the Fermi constant G_F and the electron number density n_e ,

$$V(\mathbf{x}) \approx \frac{\rho(\mathbf{x})}{\text{g/cm}^3} Y_e(\mathbf{x}) \times 7.56 \times 10^{-14} \text{eV}, \quad (2)$$

and only appears in the first element of the potential matrix in (1) for the electron flavor [28]. The matter potential $V(\mathbf{x})$ is not just proportional to the matter density $\rho(\mathbf{x})$ but also the number of electrons per nucleon $Y_e(\mathbf{x})$. Both the matter density and chemical composition vary with position. Consequently, the matter potential is in general also a function of \mathbf{x} . In the Earth crust, the electron fraction is approximately $Y_e \sim 0.5$ and the average matter density is $\bar{\rho} \equiv \langle \rho(\mathbf{x}) \rangle \approx 2.845 \text{ g/cm}^3$ [45]. For simplicity, we ignore the density variation and adopt the averaged matter density $\bar{\rho}$ as constant along the baseline of DUNE.

To make the CP and matter effect explicit, we perform a series expansion of the $\nu_\mu \rightarrow \nu_e$ ($\bar{\nu}_\mu \rightarrow \bar{\nu}_e$) oscillation probability in terms of the ratio between the two mass squared differences $\alpha \equiv \Delta m_s^2/\Delta m_a^2 \approx 3\%$ and the reactor mixing angle $s_r \equiv \sin \theta_r \approx 0.15$ [76–78],

$$P_{\nu_\mu \rightarrow \nu_e}^{\bar{\nu}_\mu \rightarrow \bar{\nu}_e} \approx \alpha^2 \sin^2 2\theta_s c_a^2 \frac{\sin^2(A\Delta_a)}{A^2} + 4s_r^2 s_a^2 \frac{\sin^2[(1 \mp A)\Delta_a]}{(1 \mp A)^2} \\ + 2\alpha s_r \sin 2\theta_s \sin 2\theta_a \cos(\Delta_a \pm \delta_D) \\ \times \frac{\sin(A\Delta_a) \sin[(1 \mp A)\Delta_a]}{A (1 \mp A)}. \quad (3)$$

The sign \pm (\mp) is for neutrino (the upper one) and anti-neutrino (the lower one), respectively. For convenience, we have used $(s_{a,r}, c_{a,r}) \equiv (\sin \theta_{a,r}, \cos \theta_{a,r})$ to denote the sine and cosine functions of the atmospheric ($\theta_a \equiv \theta_{23}$) and reactor (θ_r) mixing angles while $\theta_s \equiv \theta_{12}$ is the solar mixing angle. The matter term $A \equiv 2E_\nu V/\Delta m_a^2$ appears in two combinations, $\sin(A\Delta_a)/A$ and $\sin[(1 \mp A)\Delta_a]/(1 \mp A)$. In the limit of tiny matter effect, $A \rightarrow 0$, the two combinations reduce to approximately Δ_a and $\sin \Delta_a$, respectively. In addition, the CP phase δ_D appears as a linear combination with the atmospheric oscillation phase $\Delta_a \equiv |\Delta m_a^2|L/4E_\nu$ where L is the oscillation baseline [79].

For neutrino CP measurement, the essential observable is the difference between the neutrino and anti-neutrino oscillation probabilities, $P_{\nu_\mu \rightarrow \nu_e} - P_{\bar{\nu}_\mu \rightarrow \bar{\nu}_e} \propto \sin \Delta_a \sin \delta_D$, that is proportional to $\sin \delta_D$ in the absence of matter potential. However, a realistic measurement has sign difference in not just the Dirac CP phase δ_D but also the matter term A . With a typical size of $A \approx (0.05, 0.13, 0.21)$ estimated with the peak neutrino energies (0.55, 2, 2.5) GeV at T2K/T2HK, NO ν A, and DUNE, respectively, the matter effect on neutrino CP measurement cannot be ignored. The matter potential can fake the genuine CP violation and blur the CP measurement.

At a single long-baseline neutrino oscillation experiment, there is only one independent CP observable but two parameters (A and δ_D). To disentangle the matter contamination (A) from the genuine CP effect (δ_D), a combination of two different baselines is a promising choice. For example, the T2HKK with a 295 km baseline to the Kamioka site and a much longer baseline around 1100 km to the Korea site can effectively remove the faked CP by matter potential and achieve a better CP uncertainty [66, 67, 80, 81]. In addition, the atmospheric measurement with neutrinos produced around the Earth intrinsically has multiple baselines [60–64]. Nevertheless, the matter effect at accelerator and atmospheric neutrino oscillation experiments is not negligible in the first place. Even with multiple baselines, intrinsic uncertainty from the matter effect can still reduce the sensitivity of δ_D .

B. Improvement with μ DAR Neutrinos

A better way is significantly reducing the matter effect with low-energy neutrino beam to make $A \ll 1$ [82]. One possibility is using the muon decay at rest [83], such as DE Δ LUS [84], JUNO supplemented with μ DAR sources [85, 86], TNT2K/TNT2HK [73, 87–90], and C-ADS [91]. All these designs share the feature of multiple baselines. Especially, the TNT2K/TNT2HK configuration incorporates both low- and high-energy beams by supplementing the existing T2K/T2HK with μ SK/ μ HK (μ DAR source together with the Super-K/Hyper-K detectors) to significantly improve the CP sensitivity. The possibility of detecting μ DAR neutrinos at long baseline has also been studied but is unfortunately diluted too much over such a long baseline [92].

As mentioned above, the effect of matter potential on the neutrino oscillation is modulated by the neutrino energy. The higher neutrino energy, the larger contamination on the CP measurement. Comparing with the 30% effect at T2K for $E_\nu \approx 550$ MeV [73], DUNE with peak energy around 2.5 GeV suffers from larger matter effect. So it is more urgent for the DUNE experiment to have a complementary baseline with low-energy beam to further improve the CP measurement.

However, it is impossible to simply add a μ DAR source and share the same liquid Argon detectors of DUNE in a

similar way as TNT2K. This is because there are no free protons to provide inverse beta decay (IBD) for unique probe of the electron anti-neutrino and hence the $\bar{\nu}_\mu \rightarrow \bar{\nu}_e$ oscillation. Besides, the $\bar{\nu}_e$ -Ar cross section is too small to detect the μ DAR flux at DUNE [44].

A new THEIA detector at the same site of SURF was recently proposed [49–52, 93]. With a new technique of water-based liquid scintillator (WbLS), it is possible to use both scintillation and Cherenkov lights [94–98]. This opens the possibility of detecting the low-energy μ DAR neutrino oscillation to supplement the high-energy mode at DUNE. For convenience, we call the combination of μ DAR and THEIA as μ THEIA.

The difference between the oscillation probabilities with and without matter, $\delta P_{\mu e} \equiv P_{\mu e}(A) - P_{\mu e}(A=0)$, in Fig. 1 shows explicitly the matter effect at the DUNE and μ THEIA configurations. For DUNE ($L = 1300$ km with blue and yellow lines), the difference can be as large as $\delta P_{\mu e} \approx 0.03$ for $E_\nu/L \approx 1.5$ MeV/km which is roughly 52% (62%) of the CP-violating oscillation probability $P_{\mu e} = 0.058$ ($|P_{\mu e}^\nu - P_{\mu e}^{\bar{\nu}}| = 0.048$). Even for the neutrino energy peak at $E_\nu/L \approx 1.9$ MeV/km, the size of the matter effect is still as large as 0.025 and 33% (52%) of $P_{\mu e} = 0.075$ ($|P_{\mu e}^\nu - P_{\mu e}^{\bar{\nu}}| = 0.048$). It is interesting to see that the probability difference is almost independent of the Dirac CP phase δ_D . This is because the major matter effect, $\delta P_{\mu e} \approx 8s_r^2 s_a^2 A \approx 0.02$, comes from the second term of (3) at the oscillation peak without involving δ_D . Although the matter effect also appears through the third term of (3), the effect is further suppressed by a prefactor of $\Delta_a \sin 2\theta_s \times (\alpha/s_r) \approx 0.3$ and hence is a minor effect. Altogether, the matter effect at DUNE is at the same order as the genuine CP effect.

In contrast, the matter effect at μ THEIA ($L = 38$ km with red and green lines) is negligibly small. Being essentially insensitive to the matter potential, μ THEIA can focus on the genuine CP phase while DUNE probes both. Their combination can significantly improve the CP sensitivity. We will further discuss the details of μ THEIA and its interplay with DUNE in Sec. III for neutrino detection and Sec. IV for CP sensitivity.

III. NEUTRINO DETECTION AT THEIA AND DUNE DETECTORS

As proposed above, the essential feature of the DUNE and μ THEIA complex is a combination of different baselines and neutrino beams. In addition, the DUNE and THEIA detectors are also quite different with liquid Argon and WbLS targets, respectively. Each combination of neutrino beam and detector has its own characteristics in neutrino detection. For clarity, we elaborate separately the details of the “low-energy mode” (LEM) that the μ DAR beam is detected by the THEIA detector in Sec. III A as well as the “high-energy mode” (HEM) that the LBNF beam is detected by both the DUNE and THEIA detectors in Sec. III B. We study in detail the

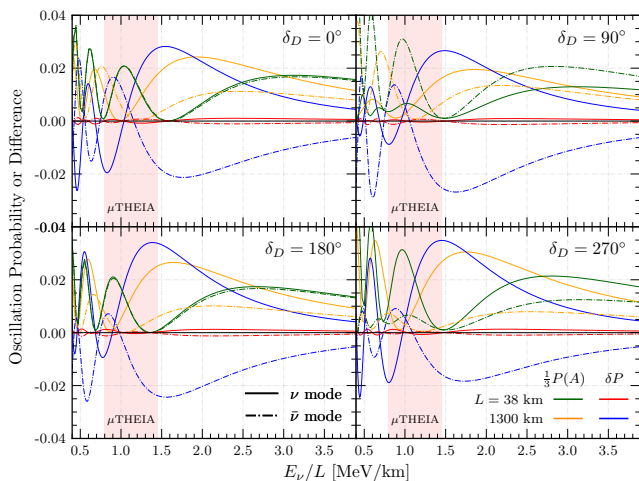


FIG. 1. The oscillation probability $\frac{1}{3}P(A)$ and oscillation probability difference $\delta P_{\mu e} \equiv P_{\mu e}(A) - P_{\mu e}(A=0)$ between the matter-induced and vacuum cases as a function of E_ν/L for both neutrino (solid) and anti-neutrino (dashed) modes. Both μ THEIA ($L = 38$ km with green line for $P_{\mu e}(A)/3$ and red one for $\delta P_{\mu e}$) and DUNE ($L = 1300$ km with yellow line for $P_{\mu e}(A)/3$ and blue one for $\delta P_{\mu e}$) are illustrated. The pink band indicates the μ THEIA energy range [30, 50] MeV while the DUNE energy window spans the whole range.

event reconstruction for both signal and background to obtain their normalized transfer tables. The event rate including the information of flux, running time, cross section, and detector size can be found in the following Sec. IV when estimating the CP sensitivity.

A. The Low-Energy Mode

The μ DAR neutrinos are produced by a cyclotron complex. For example, a typical 800 MeV proton beam hits a thick target to first generate pions. Although both π^\pm can be produced, π^- is mostly absorbed by the positively charged nuclei while π^+ decays at rest via $\pi^+ \rightarrow \mu^+ \nu_\mu$. The decay product μ^+ also loses its energy and decays at rest via $\mu^+ \rightarrow e^+ + \nu_e + \bar{\nu}_\mu$. During this process, three neutrinos (ν_μ , ν_e , and $\bar{\nu}_\mu$) are produced. Of them, $\bar{\nu}_\mu$ experiences the $\bar{\nu}_\mu \rightarrow \bar{\nu}_e$ oscillation that is of interest to CP measurement. Since μ^+ decays at rest, $\bar{\nu}_\mu$ has a well-understood spectrum with maximum energy of 53 MeV [99].

1. Signal at THEIA Detector

As mentioned in the previous section, the low-energy $\bar{\nu}_\mu$ cannot be detected by the DUNE detector. But the THEIA detector is an ideal equipment. For the major oscillation channel $\bar{\nu}_\mu \rightarrow \bar{\nu}_e$ for CP measurement with μ DAR neutrinos, the IBD process ($\bar{\nu}_e + p \rightarrow e^+ + n$) is an ideal detection method. With a large volume of

WbLS, THEIA has a significant fraction of free protons (hydrogen) to allow IBD. Both positron and neutron in the final state are detectable by THEIA.

The WbLS allows THEIA to detect both scintillation and Cherenkov lights. There are several differences between the Cherenkov and scintillation lights that can be used for separation [94, 97]: (1) the arrival time, i.e., Cherenkov light arrives nanoseconds earlier than the delayed scintillation light; (2) the angular topology, i.e., the Cherenkov light emission will cause a local enhancement on top of the isotropic scintillation signal; (3) the wavelength, i.e., the scintillation light has shorter wavelength while the Cherenkov light has relatively longer one.

For particle identification, the Cherenkov ring from e^\pm and γ has a smeared pattern. In contrast, the heavier muon or charged pion has much sharper Cherenkov ring. In addition, the production rates of Cherenkov and scintillation lights are different for different particles [94]. We will give more details once needed in later discussions.

Both Cherenkov and scintillation lights can be used for energy reconstruction. For low energy reactor and supernova $\bar{\nu}_e$ neutrinos, the energy is typically reconstructed with linear form, $E_{\bar{\nu}} = E_e + m_n - m_p$ [100] where m_n (m_p , m_e) is the neutron (proton, electron) mass and E_e the positron energy. Nevertheless, this linear formula cannot reconstruct the neutrino energy very precisely. To see the deviation clearly, we simulate the IBD events with GENIE [101, 102] and reconstruct the neutrino energy according to the linear formula. As shown in Fig. 2, the reconstructed energy spectrum for neutrinos with $E_{\bar{\nu}}^{\text{true}} = 40$ MeV spreads into a trapezoid (green solid line) and the central value shifts leftward by almost 2 MeV. In other words, for the μ DAR neutrinos with $\mathcal{O}(10$ MeV) energy, the neutrino energy reconstruction is no longer a linear dependence on the positron energy with a constant shift.

Another possibility is adding a correction term with nonlinear dependence [103],

$$E_{\bar{\nu}}^{\text{rec}} = E_e + \Delta + \frac{2E_e(E_e + \Delta) + \Delta^2 - m_e^2}{2m_p}, \quad (4)$$

where $\Delta \equiv m_n - m_p$ is the difference between the neutron (m_n) and proton (m_p) masses. The blue solid line clearly shows that the reconstructed trapezoid spectrum shifts back to center around the true neutrino energy at $E_{\bar{\nu}}^{\text{true}} = 40$ MeV. Nevertheless, the reconstructed spectrum is still a trapezoid even without smearing due to the detector resolution. With a half width being almost 1.3 MeV, the corresponding energy uncertainty can be as large as 3.25% which is even larger than the statistical uncertainty as elaborated below.

To get a precise reconstruction of the neutrino energy, we adapt the reconstruction formula from long-baseline experiments [104] to incorporate the scattering angle,

$$E_{\bar{\nu}}^{\text{rec}} = \frac{m_n^2 - m_p^2 - m_e^2 + 2m_p E_e}{2(m_p - E_e + |\mathbf{p}_e| \cos \theta_e)}, \quad (5)$$

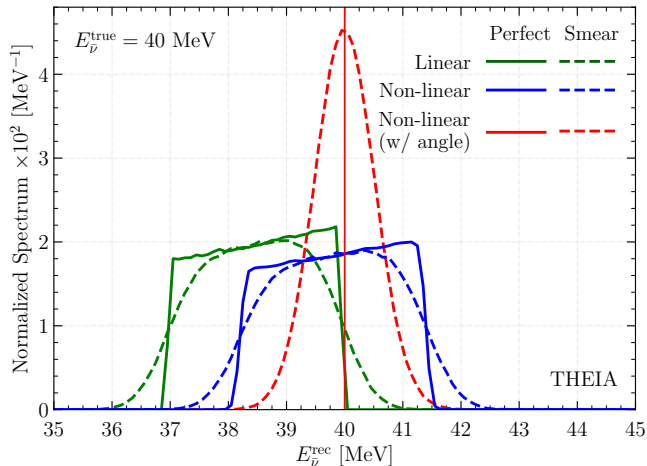


FIG. 2. The reconstructed neutrino energy $E_{\bar{\nu}}^{\text{rec}}$ spectrum of IBD events at the THEIA detector for a true energy $E_{\bar{\nu}}^{\text{true}} = 40$ MeV with linear (green) and non-linear reconstruction methods with (red) or without (blue) angular information. For comparison, both results with (dashed) and without (solid) energy smearing are shown.

where \mathbf{p}_e is the electron momentum while θ_e is the angle between the neutrino beam and positron direction. The directional information is a benefit due to the capability of detecting Cherenkov light for a WbLS detector. In the absence of detector resolution, (5) can obtain exactly the true neutrino energy and the reconstructed spectrum becomes a δ -function (red solid line) in Fig. 2. Note that the positron energy E_e cannot be directly measured. The positron not just loses its kinetic energy but also annihilates with an environmental electron to produce two 511 keV γ 's. The total deposited energy that is visible in the detector receives an extra electron mass in addition to the positron energy, $E_{\text{vis}} \equiv E_e + m_e$. In other words, the positron energy in the linear as well as non-linear energy reconstruction formula (4) and (5) is reconstructed as $E_e = E_{\text{vis}} - m_e$.

With systematical uncertainty from the reconstruction formula eliminated, the remaining uncertainty mainly comes from the detector resolutions of the visible energy E_{vis} and scattering angle θ_e . Since the light yield is proportional to the deposited energy, the visible energy E_{vis} can be reconstructed from the number of photoelectrons (p.e.) which is roughly 80 (130) p.e./MeV for the Cherenkov (scintillation) light [97]. The relative statistical uncertainties are $(\sigma_{E_{\text{vis}}}/E_{\text{vis}})_{\text{Ch}} = 1/\sqrt{80 \times E_{\text{vis}}/\text{MeV}}$ for the Cherenkov light and $(\sigma_{E_{\text{vis}}}/E_{\text{vis}})_{\text{sc}} = 1/\sqrt{130 \times E_{\text{vis}}/\text{MeV}}$ for the scintillation light, respectively. The combined uncertainty is

$$\frac{\sigma_{E_{\text{vis}}}}{E_{\text{vis}}} = \frac{1}{\sqrt{210 \times E_{\text{vis}}/\text{MeV}}} \approx \frac{7\%}{\sqrt{E_{\text{vis}}/\text{MeV}}}. \quad (6)$$

Since the μDAR neutrino energy is typically $\mathcal{O}(10 \text{ MeV})$,

the relative error $\sigma_{E_{\text{vis}}}/E_{\text{vis}} \lesssim 2\%$ is actually quite good. Note that the scintillation light yield is more efficient than the Cherenkov one and both can play important roles in energy reconstruction. At $E_{\bar{\nu}}^{\text{true}} = 40$ MeV, the positron energy resolution leads to about 1.17% uncertainty on the reconstructed neutrino energy.

In addition, the scattering angle θ_e in (5) also receives an imperfect detector resolution and blur the reconstructed neutrino energy. Although the actual resolution for the μDAR flux that has higher energy should be better, we take a conservative value $\sigma_{\theta} = 10^\circ$ [51] estimated for supernova neutrino. The angular uncertainty leads to a 0.44% uncertainty on the neutrino energy reconstruction which is slightly less than the one from positron energy resolution. In Fig. 2, the dashed lines show the combined neutrino energy uncertainty, which is 1.28% for $E_{\bar{\nu}}^{\text{true}} = 40$ MeV assuming Gaussian smearing.

Once produced, the neutron from IBD would experience thermalization and lose energy before being captured. The scintillation light emitted during this process can mix with the light from positron. Consequently, the visible energy receives an extra contribution from the neutron kinetic energy T_n , $E_{\text{vis}} = E_e + m_e + Q_F \times T_n$ where Q_F is the neutron quenching factor. For the μDAR neutrino at 40 MeV, the neutron kinetic energy T_n is typically 3 MeV according to GENIE simulation. With WbLS, it is possible to reconstruct the neutron kinetic energy T_n by measuring the positron scattering angle [105]. The neutron quenching factor Q_F keeps decreasing with T_n and is 15% at $T_n = 0.25$ MeV [105]. Then from the measured visible energy E_{vis} , one can first solve the positron energy $E_e = E_{\text{vis}} - m_e - Q_F \times T_n$ and put it into (5) to reconstruct $E_{\bar{\nu}}$. In principle, the neutron kinetic energy is not a problem for the IBD energy reconstruction. But the neutron quenching factor Q_F still remains to be measured in a WbLS as far as we know. So for simplicity, we omit the neutron kinetic energy in our current phenomenological study.

2. Background Suppression with WbLS

As illustrated in Sec. III A 1, the $\bar{\nu}_e$ signal contains not just a positron but also a neutron in the final state. Although a single positron can already allow precise energy reconstruction, it receives various backgrounds. The final-state neutron is extremely important for selecting out the IBD signal with double coincidence.

The neutron is produced at the same time as the positron. But the neutron signal comes out much later with a delay of 250 μs [106]. Since the time resolution required to separate the Cherenkov and scintillation lights (typically 0.1 ns) is much smaller [51], the delayed neutron signal can be well separated from the positron one. When neutron is captured by nuclei, the delayed γ s also produce e -like Cherenkov rings and scintillation lights to allow neutron tagging at THEIA [106]. The neutron tagging efficiency can reach almost 90% [107].

The double coincidence requiring both positron and neutron signals can remove those events that contain only one faked positron. But there are still various backgrounds that can survive [87, 108] including the beam neutrinos from the complementary high-energy beam neutrinos, the low-energy reactor, solar and supernova neutrinos, the intrinsic beam neutrinos from the same μ DAR flux, as well as the atmospheric neutrinos. The invisible muon decay from atmospheric neutrinos is particularly difficult to remove since both positron and neutron can be produced to fake the signal. Fortunately, the new technique of WbLS can be very efficient in suppressing these backgrounds as we elaborate below.

Reactor, Solar, Geo-, Supernova, and DUNE Beam Neutrinos – At low energy, there are four neutrino sources from reactor [109, 110], solar [111], geo-radioactivity [112, 113], and supernova [114, 115]. While the solar neutrinos are not anti-neutrinos and hence cannot fake the $\bar{\nu}_e$ IBD signal, the other three may be incorrectly identified as the signal. Fortunately, all these neutrinos typically have much lower energy than majority of the μ DAR neutrinos. With an energy cut, $E_{\bar{\nu}} > 30$ MeV, they can be safely removed [87]. On the other side, the LBNF beam can also contribute $\bar{\nu}_e$ flux. With pulsed beam at much higher energy, a combined cut on the arrival time and energy, $E_{\bar{\nu}} < 55$ MeV, will eliminate the contamination from the complementary DUNE experiment.

Intrinsic μ DAR Beam – During the production of μ DAR with cyclotron, various neutrinos can be produced via $\pi^\pm \rightarrow \mu^\pm + \nu_\mu(\bar{\nu}_\mu)$ and $\mu^\pm \rightarrow e^\pm + \bar{\nu}_\mu(\nu_\mu) + \nu_e(\bar{\nu}_e)$. One needs to examine all possible intrinsic backgrounds. The $\bar{\nu}_e$ flux can produce exactly the same IBD signal and becomes an intrinsic background from the same μ DAR source. There is no way to remove or suppress this background on the detector side. Fortunately, the negatively charged π^- is efficiently absorbed by the positively charged nuclei inside the target before decay. So the μ^- production is much smaller than μ^+ with a suppression as large as 10^{-4} [87]. Since the $\bar{\nu}_\mu \rightarrow \bar{\nu}_e$ oscillation probability is typically $\mathcal{O}(1\%)$ and hence two orders larger, the μ^- contamination can be safely neglected.

The second beam background is the electron neutrino ν_e from the same μ DAR. After oscillation, most ν_e neutrinos can survive and scatter with oxygen ($\nu_e + {}^{16}\text{O} \rightarrow e^- + {}^{16}\text{F}$) or carbon ($\nu_e + {}^{12}\text{C} \rightarrow e^- + {}^{12}\text{N}$)¹ to produce an electron in the final state. Fortunately, the scattering cross section with oxygen is much smaller than the IBD one in the μ DAR energy range [116, 117] and hence can be neglected. Even if some events can still be produced, the double coincidence of neutron capture can remove this background.

The muon neutrino and anti-neutrino cannot experi-

ence charged-current scattering with not enough energy to produce a μ^\pm in the final state. However, all neutrinos and anti-neutrinos can elastically scatter with electron to produce an energetic electron in the final state. But these backgrounds can also be removed by requiring neutron capture [94, 97].

Atmospheric Neutrinos – The atmospheric neutrino flux [118, 119] contains all neutrino flavors ($\nu_e, \bar{\nu}_e, \nu_\mu, \bar{\nu}_\mu, \nu_\tau, \bar{\nu}_\tau$) to contribute as background [87]. With much higher energy, the atmospheric neutrino backgrounds can experience all types of neutrino-nucleus scattering and hence need much more dedicated treatment. Fortunately, the excellent performance of the WbLS with both Cherenkov and scintillation detection can effectively suppress these backgrounds. Except $\bar{\nu}_e$ and $\bar{\nu}_\mu$, the other components can be removed at the THEIA detector as we elaborate below.

ν_e : The charged-current quasi-elastic scattering (CC-QES) process $\nu_e + {}^{16}\text{O} \rightarrow e^- + {}^{16}\text{F}$ cannot produce a neutron. Then the neutron tagging with WbLS can efficiently remove this background. For the atmospheric ν_e with higher energies, 30% of the CC-QES scattering process can kick out a neutron and a proton from the nuclei via $\nu_e + {}^{16}\text{O} \rightarrow e^- + n + {}^{15}\text{O}^* + p$. Since energy is needed to kick out n and p , the primary electron energy is much smaller than the neutrino energy. Mainly $E_\nu \in [80, 130]$ MeV will produce electrons with energy reconstructed in the μ DAR range [30, 55] MeV. In addition, roughly half of the single neutron events are also accompanied by a monoenergetic photon (~ 6.2 MeV) due to the de-excitation of ${}^{15}\text{O}^*$, which can also serve as background veto. Both electron (T_e) and proton (T_p) kinetic energies deposit as visible energy E_{vis} . Requiring $E_{\text{vis}} \in [30, 55]$ MeV, only 0.07 events per year at THEIA-25 can survive, which is a negligible amount.

Moreover, those neutrinos with even higher energy can also have resonant (RES) and deep inelastic (DIS) scatterings with at least a pion (π^0 or π^+) starting around $E_\nu \approx 200$ MeV, and possibly a neutron in the final state. In addition, the interaction can also produce protons in the final state or kick off protons from the nucleus [120]. The neutron capture process emits a single 2.2 MeV photon [97] that can be used to separate RES and DIS events. In the energy range $E_\nu \in [200, 600]$ MeV that can contribute to the μ DAR IBD energy window, roughly 30% of CC-RES can have a single neutron. The events containing π^0 can be vetoed by energy cut $E_{\text{vis}} < 55$ MeV, since the π^0 decays immediately into a pair of photons each with energy $E_\gamma \geq m_\pi/2$. This reduces the remaining atmospheric ν_e background by another 50% to only 15% of the total CC-RES. The charged π^+ first deposits its kinetic energy as scintillation light and then decays at rest to produce a μ^+ , since its decay length is typically at least one order longer than the radiation length in

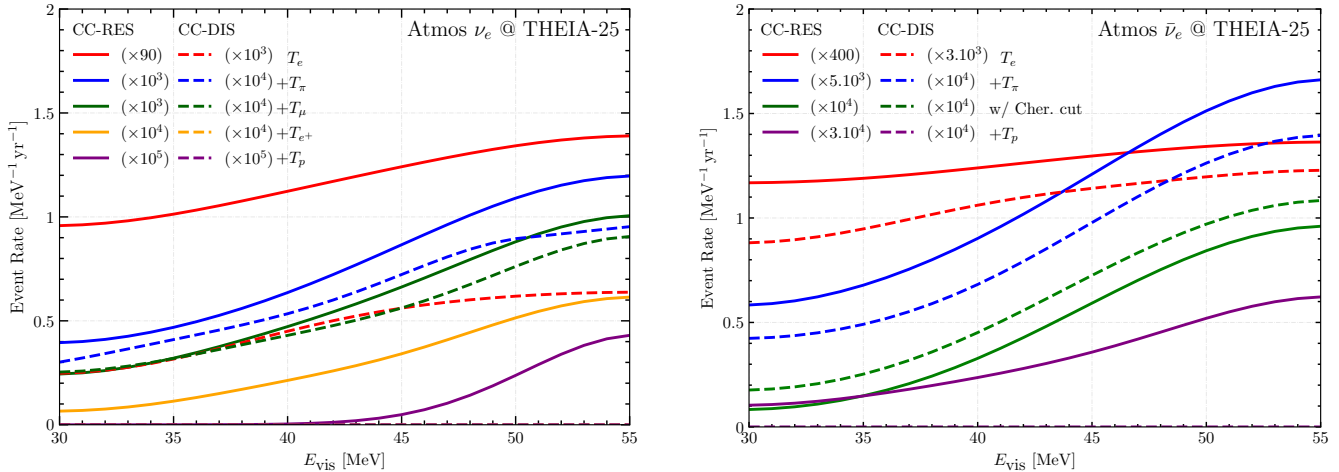


FIG. 3. The atmospheric ν_e (left) and $\bar{\nu}_e$ (right) background event rate spectrum from CC-RES (solid) and CC-DIS (dashed) interactions as a function of the visible energy E_{vis} at THEIA-25. With energy deposits from the primary electron (T_e , red), charged π^+ ($+T_\pi$, blue), μ^+ ($+T_\mu$, green), the Michel electron ($+T_{e^+}$, yellow), and proton ($+T_p$, purple) gradually added up, the ν_e event spectrum moves out of the IBD energy window [30, 55] MeV to higher energy. Similarly, the $\bar{\nu}_e$ spectrum has the same feature with the primary electron (T_e , red), charged π^- ($+T_\pi$, blue) or with Cherenkov cut (w/ Cher. cut, green), and proton ($+T_p$, purple). Multiplication factors have been used to make the highly suppressed spectrum visible.

water [121]. Then the energy deposition is composed of five parts: 1) the kinetic energy T_e of the primary electron; 2) the proton kinetic energy $T_p \equiv E_p - m_p$; 3) the π^+ kinetic energy $T_\pi \equiv E_\pi - m_\pi$; 4) the μ^+ kinetic energy $T_\mu = (m_\pi - m_\mu)^2/2m_\pi \approx 4\text{ MeV}$ that is uniquely determined by the pion decay at rest; and 5) the e^+ energy T_{e^+} ranging from 0 to $m_\mu/2$. Since the positron always annihilates with an environmental electron, we also include the released $2m_e$ photon energy in T_{e^+} for convenience. For a π^+ with energy E_π , the minimal total energy deposit is $E_\pi - m_\pi + T_\mu + 2m_e \approx E_\pi - 134\text{ MeV}$ if both the primary and Michel electrons have vanishing momentum. Those events with $E_\pi \gtrsim 189\text{ MeV}$ can be vetoed by $E_{\text{vis}} \geq 55\text{ MeV}$. Requiring the primary and Michel electrons to be produced at rest is actually very stringent. Even with less energetic π^+ , the atmospheric ν_e background can be easily vetoed. As shown in the left figure of Fig. 3, once the π^+ , μ^+ , and e^+ energies are considered, the ν_e CC-RES event rate is suppressed to negligible level with just around 8×10^{-4} events/year for $E_{\text{vis}} \in [30, 55]\text{ MeV}$ at the THEIA-25 detector. Fig. 3 also shows the CC-DIS case which has only 20% for single neutron events and its contribution is only around 10^{-5} event per year. The typical value of the proton kinetic energy is around $\mathcal{O}(10\text{ MeV})$ for sub-GeV neutrinos. It can further suppress the background by one order

for RES and almost down to zero for DIS, shown as the purple curves of Fig. 3.

$\bar{\nu}_e$: The electron anti-neutrino $\bar{\nu}_e$ that scatters with Hydrogen via CC-QES (or precisely IBD) process is an irreducible background to the IBD signal and there is no experimental solution. It contributes the major background for μ THEIA. Since the direction of the incoming $\bar{\nu}_e$ is unknown, the scattering angle θ_e in (5) cannot be correctly measured but only inferred from the μ DAR source direction. This *wrong scattering angle effect* introduces significant smearing for the reconstructed neutrino energy $E_{\bar{\nu}}$. With more details elaborated in App. A, Fig. 4 shows that the smearing can be as large as $3.4\% \sim 5.5\%$ at half height for $E_\nu \in [30, 55]\text{ MeV}$. The wrong scattering angle effect is much larger than the detector resolution in Fig. 2 with known direction. With higher neutrino energy, the wrong scattering angle effect becomes more severe. The atmospheric $\bar{\nu}_e$ CC-QES background is estimated as 1.1 event per year at THEIA-25.

The $\bar{\nu}_e$ CC-RES and CC-DIS events mainly consist of a π^0 or π^- in addition to the primary positron. Slightly higher than the ν_e mode, the single neutron events contribute around 50% (60%) of the total CC-RES (CC-DIS) events. The π^0 can be vetoed by the energetic photon with $E_\gamma \geq m_\pi/2$. Since the pion decay length is much longer than its radiation length in water, π^- first loses its kinetic energy and then is absorbed by the positively charged nuclei. The minimal energy deposit is then only its kinetic energy $T_\pi = E_\pi - m_\pi$ and no μ^- or subsequent electron from μ^- decay. For comparison with the ν_e mode, the deposited E_{vis} is shown in the right panel of Fig. 3. As mentioned earlier, 80 (130) photoelectrons

¹ Since the scintillator composition and fraction for THEIA are not decided yet and only a possible fraction $1\% \sim 10\%$ is mentioned [51], we leave the carbon contribution open and focus on the major water target.

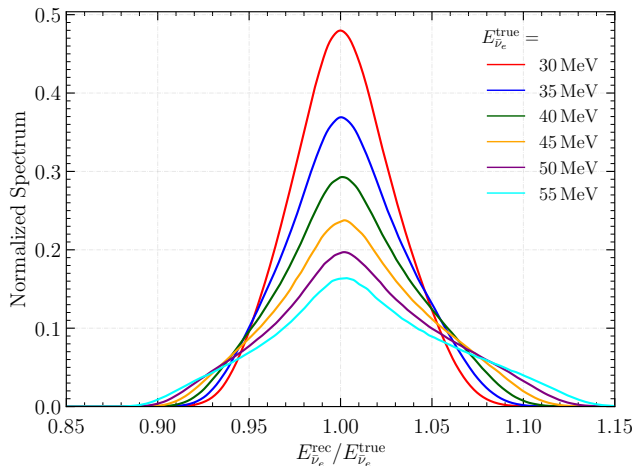


FIG. 4. The wrong scattering angle effect on the reconstructed neutrino energy E_{ν}^{rec} for the atmospheric $\bar{\nu}_e$ background in the unit of the corresponding true neutrino energy $E_{\nu_e}^{\text{true}}$. Several typical neutrino energies, $E_{\nu_e}^{\text{true}} = 30$ MeV (red), 35 MeV (blue), 40 MeV (green), 45 MeV (yellow), 50 MeV (purple), and 55 MeV (cyan), are shown for comparison.

can be produced for each MeV energy deposit [97] as Cherenkov (scintillation) lights. So the required μ DAR energy window [30, 55] MeV corresponds to [2400, 4400] Chereknov photons and [3900, 7150] scintillation ones, respectively. The atmospheric $\bar{\nu}_e$ CC-RES (CC-DIS) background only contributes 1.2×10^{-3} (1.5×10^{-3}) event per year at THEIA-25. This is negligibly small compared with the atmospheric $\bar{\nu}_e$ CC-QES background with 1.1 events per year. This background is further suppressed to 1/4 for the RES and almost 0 for the DIS processes if the proton kinetic energy is considered.

$\nu_{\mu}/\bar{\nu}_{\mu}$: For the atmospheric muon neutrinos $\nu_{\mu}/\bar{\nu}_{\mu}$, the charged-current scattering produces a μ^{\mp} in the final state. If the muon energy is above the Cherenkov threshold, the μ -like ring has different pattern to be distinguished from the e -like one. In addition, the ratio between the Cherenkov (N_{ch}) and scintillation (N_{sc}) lights is also quite different between electron ($N_{\text{ch}}/N_{\text{sc}} \approx 0.2$) and muon ($N_{\text{ch}}/N_{\text{sc}} \lesssim 0.08$) rings [94].

On the other hand, the Cherenkov light alone cannot see an “invisible muon” below the Cherenkov threshold but only its decay product e^{\pm} [87]. Fortunately, with a muon lifetime of $2.2 \mu\text{s}$, the time resolution (~ 0.1 ns) of WbLS is good enough to separate the muon scintillation light from the e^{\pm} Cherenkov and scintillation lights [94]. In other words, the WbLS can identify the invisible muon with triple coincidence (μ scintillation light, e^{\pm} Cherenkov and scintillation lights, and the 2.2 MeV delayed γ from neutron capture). The triple coincidence can essentially remove all the invisible muon background. Even for a conservative study by requiring the Cherenkov photon and the combined scintillation photon to satisfy $N_{\text{ch}}/N_{\text{sc}} > 0.4$, the background rate is suppressed to only

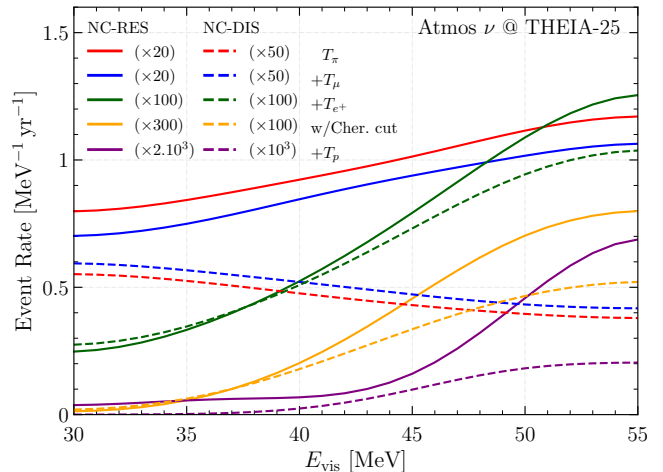


FIG. 5. The background event rate spectrum of the atmospheric NC-RES (solid) and NC-DIS (dashed) events as a function of the visible energy E_{vis} with one year running at THEIA-25. For comparison, the deposited energies of pion (T_{π} , red), muon ($+T_{\mu}$, blue), positron ($+T_{e^+}$) without (green) or with (yellow) Cherenkov cut, and proton ($+T_p$, purple) are added up step by step. To put all curves at similar heights, multiplication factors are implemented accordingly.

2% [94].

$\nu_{\tau}/\bar{\nu}_{\tau}$: Although tau neutrinos also exist in the atmospheric flux, the primary τ^{\pm} from the CC scattering can decay into either electron or muon with roughly 17% branching ratio each. However, the τ^{\pm} lepton is very heavy with mass at 1.78 GeV. The electron and muon from tau decay is then much more energetic than the IBD signal. A simple cut on the visible energy can effectively veto the atmospheric tau neutrino backgrounds.

Neutral Current: In addition to the CC events, the neutral-current (NC) scattering is also a potential background. Since the neutral current process is flavor blind, all flavors can contribute. First, the NC-QES scattering can not contribute as background since there is no positron in the final state. The NC-RES and NC-DIS processes both allow a single π^{\pm} and π^0 production in the final state. The interaction can also produce neutron and proton. Since π^0 decays into a pair of photons each with energy larger than $m_{\pi}/2 \approx 70$ MeV, the deposit energy is already beyond the IBD window of μ DAR $\bar{\nu}_e$. Among the remaining π^{\pm} , π^{-} is absorbed by nuclei and only π^{+} below Chereknov threshold can decay through $\pi^{+} \rightarrow \mu^{+} \rightarrow e^{+}$ to fake the IBD positron. For NC-RES (NC-DIS) events, around 43% (45%) have a single neutron while 16% (22%) have a single charged π^{+} in the final state. The fraction reduces to 11% (18%) if requiring both neutron and π^{+} . It has a probability for E_{vis} being within the energy window of interest as shown in Fig. 5. Requiring $E_{\text{vis}} \in [30, 55]$ MeV, the integrated event number gives around 0.03 (0.06) events per year for NC-RES (NC-DIS) at THEIA-25 which is also a negligible amount. Since there is also proton, the background

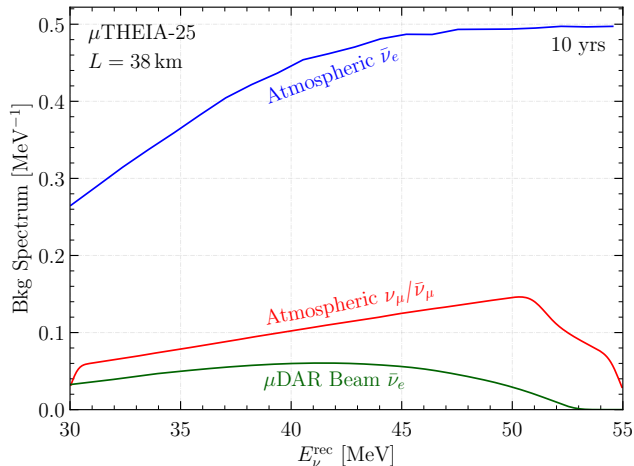


FIG. 6. The major background spectrum to the μ DAR IBD signal as a function of the reconstructed neutrino energy E_ν^{rec} at THEIA-25 (17 kt) with 10 years running and a baseline of $L = 38$ km. The remaining backgrounds are atmospheric $\bar{\nu}_e$ (blue), invisible muon (red), and the μ DAR $\bar{\nu}_e$ (green).

can be further reduced by at least one order if the proton kinetic energy is also taken into account.

Fig. 6 shows the three survival background spectra as discussed above, including the beam $\bar{\nu}_e$ with 1.83×10^{25} protons on target (POT) as well as the atmospheric $\bar{\nu}_e$ and $\nu_\mu/\bar{\nu}_\mu$. While the atmospheric invisible muon background dominates at a Cherenkov detector such as Super-K and Hyper-K [87], it is a small minor contribution at the WbLS detector THEIA even with a conservative selection procedure. The intrinsic μ DAR beam background is even smaller. THEIA is an ideal detector for the CP measurement with μ DAR source.

3. Event Selection

As elaborated above, the IBD signal is quite distinctive at the THEIA detector. All backgrounds can be suppressed to negligibly small amount. Here we summarize the selection criteria for the IBD events,

- (1) Only one e -like Cherenkov ring;
- (2) For the total visible energy E_{vis} , the number of scintillation photons N_{sc} is within the range of [3900, 7150] and Cherenkov photons $N_{\text{ch}} \in [2400, 4400]$ that correspond to a (30 \sim 55) MeV positron;
- (3) The ratio of Cherenkov and scintillation photons $N_{\text{ch}}/N_{\text{sc}}$ is larger than 0.4;
- (4) Existence of delayed γ s from neutron capture;

For the above requirements, the energy window used in the criterion (2) can remove reactor, solar, geo-, supernova and DUNE beam neutrino backgrounds. The cri-

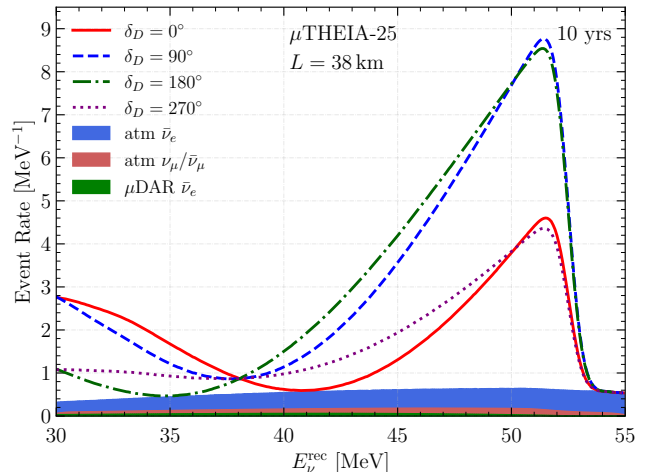


FIG. 7. The event spectra of μ DAR source at THEIA detector at baseline $L = 38$ km. The Four solid lines are $\delta_D = 0^\circ$ (red), 90° (blue), 180° (green), and 270° (purple). The filled regions stand for the backgrounds the atmospheric $\bar{\nu}_e$ (blue), the atmospheric $\nu_\mu/\bar{\nu}_\mu$ (red) and the intrinsic $\bar{\nu}_e$ from the μ DAR beam (green).

teria (2) and (4) as double coincidence is efficient in removing the μ DAR flux background except the intrinsic $\bar{\nu}_e$. The combination of all criteria forms the triple coincidence which is even more powerful to reduce the invisible muon background. Finally, the criteria (1) and (2) can remove the atmospheric CC-RES, CC-DIS, and NC backgrounds.

Note that these criteria are already quite conservative. For the WbLS technique to be used by THEIA, more information can help to distinguish signal from background. Especially, the time information and pulse shape can be used to distinguish the Cherenkov and scintillation lights [94]. This could be extremely useful to further suppress the atmospheric invisible muon background with triple coincidence fully implemented.

In Fig. 7, we show the signal and background event rates for the low-energy mode at μ THEIA. The WbLS can highly suppress the background especially for the “invisible muon” that is reduced to a negligible amount. With CP dependence dominating the event rate, we can expect improvement of the CP sensitivity, which is elaborated later in Sec. IV.

B. The High-Energy Mode

The high-energy LBNF neutrinos from Fermilab to SURF is a wide beam spanning from 0.5 GeV to 5 GeV with peak at 2.5 GeV [44] for both neutrino and anti-neutrino modes. Each mode contains four different flavor components: ν_e , $\bar{\nu}_e$, ν_μ and $\bar{\nu}_\mu$. Since the THEIA detector is at the same SURF experimental site as the DUNE far detectors, it can also probe the LBNF neutrinos. While the event reconstruction of high energy neu-

trinos at the DUNE liquid Argon detectors has already been studied carefully [122], we focus on the detection at THEIA.

The key element for the neutrino CP measurement is neutrino flavor reconstruction for $\nu_\mu \rightarrow \nu_e$ ($\bar{\nu}_\mu \rightarrow \bar{\nu}_e$). It is interesting to see that the low-energy μ DAR neutrinos outside the energy window [0.5 GeV, 5 GeV] cannot contribute as background. Although atmospheric neutrinos can overlap in energy, the pulse shape of the LBNF beam provides an efficient way to suppress the atmospheric backgrounds. Both signal and the remaining background actually come from the same LBNF beam.

With broad energy range, several types of CC scatterings with a target nuclei N can happen. In addition to a charged lepton ℓ_α , the final state is either a single nuclei N' for the quasi-elastic ($\nu_\alpha + N \rightarrow \ell_\alpha + N'$), nuclei plus mesons for the resonant ($\nu_\alpha + N \rightarrow \ell_\alpha + N' + meson$), or nuclei plus hadrons for the deep-inelastic ($\nu_\alpha + N \rightarrow \ell_\alpha + N' + hadrons$) CC scatterings [117]. Typically CC-QES dominates below 1 GeV and CC-RES between 1.2 GeV and 5 ~ 7 GeV, while CC-DIS takes over above 7 GeV. With the LBNF neutrino beam being below 5 GeV, most of the interactions are CC-QES and CC-RES. In order to make better neutrino reconstruction, it is desirable to distinguish these different CC scattering events.

The following discussions focus on the signal of appearance channels $\nu_\mu \rightarrow \nu_e$ and $\bar{\nu}_\mu \rightarrow \bar{\nu}_e$. Similar procedures shall also apply for the disappearance channels $\nu_\mu \rightarrow \nu_\mu$ and $\bar{\nu}_\mu \rightarrow \bar{\nu}_\mu$. Although the disappearance channels do not contribute significantly to the leptonic CP measurement, they can serve as supplementary probe of the other oscillation parameters and the neutrino flux. Both appearance and disappearance channels are taken into account in our GLOBES simulation in Sec. IV.

1. The CC-QES Category

Signals – The CC-QES process has a two-body final state with a primary lepton and a nuclei. A combination of Cherenkov and scintillation lights can achieve outstanding lepton identification as discussed in Sec. III A. Similar to the IBD case (5), the neutrino energy can be reconstructed from the charged lepton energy E_ℓ (or momentum $|\mathbf{p}_\ell|$) and scattering angle θ_ℓ [104],

$$E_\nu^{\text{rec}} = \frac{m_f^2 - (m'_i)^2 - m_\ell^2 + 2m'_i E_\ell}{2(m'_i - E_\ell + |\mathbf{p}_\ell| \cos \theta_\ell)}, \quad (7)$$

where m_f is the final-state nucleon mass. On the other hand, the initial nucleon mass m_i always appears together with the binding energy E_b for a nucleon inside ^{16}O nuclei as $m'_i \equiv m_i - E_b$. The binding energy $E_b = 42$ MeV (19 MeV) for the neutrino (anti-neutrino) mode is adopted to make the reconstructed energy peak at the true value for $E_\nu = 2.5$ GeV as shown in Fig. 8. This energy reconstruction formula is similar to the IBD one (5) with the only difference that the initial free proton

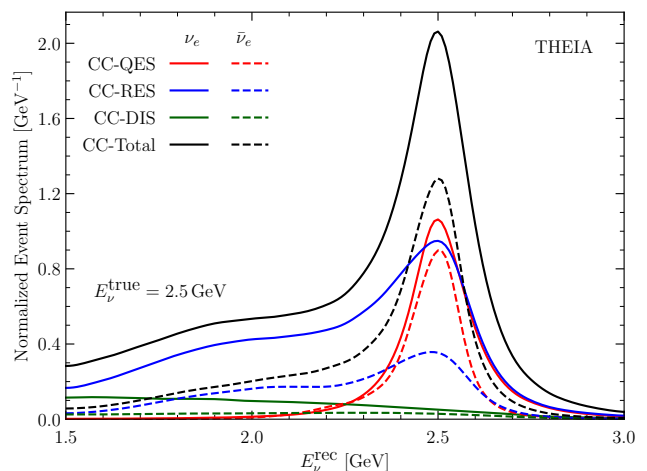


FIG. 8. The reconstructed energies of a 2.5 GeV $\nu_e/\bar{\nu}_e$ neutrino at the THEIA detector for different CC scattering processes: QES (red), RES (blue), and DIS (green). The combined total spectrum is plotted in black color. For comparison, both ν_e (solid) and $\bar{\nu}_e$ (dashed) modes are plotted. Note that the total spectrum for neutrino mode is normalized and the others weighted by their corresponding cross sections.

(Hydrogen) mass m_p is replaced by m'_i to account for the binding energy. Experimentally, there is no efficient way to distinguish whether it is the Oxygen or Hydrogen nuclei that is scattered. Consequently, the neutrino energy reconstruction (7) for Oxygen target is used universally since the mass fraction of Oxygen is eight times larger than Hydrogen in the water target. Similar to the low energy mode, the same Gaussian smearing $7\%/\sqrt{E_{\text{vis}}/\text{MeV}}$ is used for simulating the detector resolution of the deposit visible energy. In addition, we take the angular resolutions 1.48° for e^\pm and 1.00° for μ^\pm from SK-IV [123].

Fig. 8 shows the reconstructed spectrum for a 2.5 GeV ν_e ($\bar{\nu}_e$) at the THEIA detector. For the CC-QES events, the reconstructed neutrino energy spectrum is the narrowest whose width at half height is roughly 80 MeV. The high-energy CC-RES or CC-DIS event always has at least one π^\pm/π^0 in the final state which can be used to distinguish from the CC-QES signal. That means the CC-QES events can be separated from the CC-RES and CC-DIS counterparts. For illustration, Fig. 8 also shows the individual features of CC-RES and CC-DIS events separately. The fact that CC-RES and CC-DIS partially overlap with each other will be elaborated in later discussions.

Backgrounds – The LBNF beam can contribute intrinsic ν_e ($\bar{\nu}_e$) background $\nu_e \rightarrow \nu_e$ ($\bar{\nu}_e \rightarrow \bar{\nu}_e$) which is irreducible. For the neutrino (anti-neutrino) mode, the ν_e ($\bar{\nu}_e$) flux is two orders smaller than the dominant ν_μ ($\bar{\nu}_\mu$) [122]. Considering the $\nu_\mu \rightarrow \nu_e$ ($\bar{\nu}_\mu \rightarrow \bar{\nu}_e$) oscillation probability that is typically $\lesssim 5\%$, the intrinsic background can be comparable or roughly one order smaller

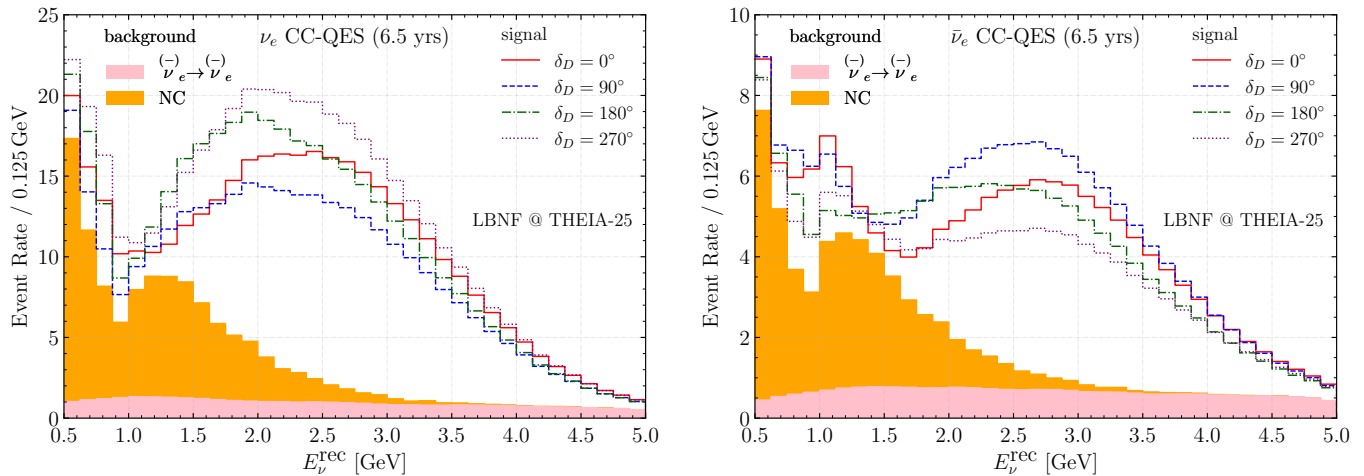


FIG. 9. The LBNF CC-QES signal (lines) and background (filled regions) event spectra as functions of the reconstructed neutrino energy E_{ν}^{rec} at the THEIA-25 detector. Both neutrino (left) and anti-neutrino (right) modes are shown, each with 6.5 years running. The signal curves adopts four different values of the Dirac CP phase $\delta_D = 0^\circ$ (red), 90° (blue), 180° (green), and 270° (purple) to make comparison. On the other hand, the background is divided into CC (pink) and neutral current (NC, yellow) components.

than the signal. In other words, the intrinsic beam background is sizable and hence cannot be neglected. Moreover, the beam also has intrinsic $\bar{\nu}_e$ (ν_e) fluxes which are smaller by another order. Although the positron annihilation at the THEIA detector can in principle be used to distinguish the electric charge of the final-state leptons, we assume the $\bar{\nu}_e$ (ν_e) also contributes as background to be conservative. The intrinsic beam backgrounds are shown as the pink filled region in Fig. 9.

For the disappearance channel of ν_μ ($\bar{\nu}_\mu$), the misidentification of muon as electron is also a potential background. Nevertheless, the misidentification rate is 0.05% for a muon misidentified as an electron and 0.02% for the converse one [123]. This contribution is much smaller than the intrinsic $\nu_e/\bar{\nu}_e$ background and hence can be neglected for simplicity.

As for the neutral-current events, the NC-QES does not have charged lepton in the final state which can serve as an effective veto. However, the NC-RES and NC-DIS scatterings have both single and multi-pion final states. The multi-pion background can be removed by simply imposing a single-ring cut. Single pion production has π^\pm or π^0 in the final state. The π^\pm above the Cherenkov threshold can produce a μ -like ring, since both are heavy particles with similar masses. For π^+ below the Cherenkov threshold, it can experience a chain decay $\pi^+ \rightarrow \mu^+ \rightarrow e^+$ with both π^+ and μ^+ decaying at rest. Although the final e^+ can produce an e -like ring, its maximal energy is only $m_\mu/2 = 53$ MeV and hence the reconstructed energy is far below the signal energy window $[0.5, 5]$ GeV. Moreover, the invisible π^+ and μ^+ can actually be seen by the THEIA detector with scintillation lights before the e^+ Cherenkov ring,

which provides an extra way to veto the invisible π^+ background. Furthermore, the invisible π^- is absorbed in the detector and hence cannot produce an electron to fake signal. Neither π^+ nor π^- can become background. However, the photon pair from π^0 decay can fake an electron. This happens if (1) the two photons have a small opening angle $\theta_{\gamma\gamma} \leq 17^\circ$ and overlap with each other or (2) one photon is soft enough to be invisible [124]. Roughly 3.3% (16.2%) of NC-RES (NC-DIS) single π^0 events at the peak energy $E_\nu = 2.5$ GeV have overlapping photons. For the soft photon in case (2), we take a conservative $E_\gamma < 30$ MeV Cherenkov detection threshold [124]. The soft photon events with $\theta_{\gamma\gamma} > 17^\circ$ contribute 7.6% (6.8%) of the NC-RES (NC-DIS) scatterings. In total, 10.9% (23.0%) of the NC-RES (NC-DIS) events have a π^0 to fake the electron. The π^0 direction and energy are then used as the electron information to reconstruct the neutrino energy via (7) for small opening angle case. Since the soft photon direction is difficult to reconstruct, the direction of the hard photon is used instead.

Event Selection – As elaborated above, the CC-QES category has only one primary lepton in the final state. Being different from the IBD signal of the low-energy mode, there is no neutral for double coincidence to significantly suppress the background. The selection criteria for the CC-QES signal events are summarized below,

- (1) Only one primary e -like Cherenkov ring with $|\mathbf{p}_e| > 100$ MeV. For the disappearance channel the primary muon is selected with μ -like Cherenkov ring with $|\mathbf{p}_\mu| > 200$ MeV.

- (2) Reconstructed neutrino energy inside the range [0.25, 5] GeV.
- (3) No extra Cherenkov light from mesons.

The event spectra of the CC-QES category after selection and the corresponding backgrounds are shown as functions of the reconstructed neutrino energy E_ν^{rec} in Fig. 9. For both neutrino and anti-neutrino modes, the signal lines clearly show the CP dependence. Taking $\delta_D = 90^\circ$ for illustration, the corresponding blue line is at the bottom for the neutrino mode while it is at the top for the anti-neutrino one. The opposite feature happens for the other maximal CP phase $\delta_D = 270^\circ$. This is a reflection of the fact that the CP-violating term $\sin \delta_D$ in (3) differs by a sign. The NC background is contributed by all flavors and the CC one by the intrinsic $\nu_e/\bar{\nu}_e$ beam background in addition to the misidentified $\nu_\mu/\bar{\nu}_\mu$ comes from the disappearance channels. While the signal and CC backgrounds can extend to 5 GeV, the NC background mainly contributes below 3.5 GeV since typically more particles are produced to split the energy. The two NC background peaks here are produced due to the soft photon contribution (lower energy peak) and the small opening angle contribution (higher energy peak), respectively. For CC-QES, the CC background spectrum is quite flat and the NC backgrounds dominate below 2.5 GeV. Around the peak energy, $E_\nu^{\text{rec}} = 2.5$ GeV, the signals dominate to provide a good CP sensitivity. Between neutrino and anti-neutrino modes, the typical event rate differs by a factor around 2.5.

2. The CC-RES Category

Signals – The CC-RES process for the appearance signal $\nu_\mu \rightarrow \nu_e$ ($\bar{\nu}_\mu \rightarrow \bar{\nu}_e$) has 1 electron (positron) plus 1 pion (π^\pm or π^0). Therefore, the CC-RES event can be distinguished from the CC-QES one by ring counting if the final-state pion is a charged one π^\pm . For π^0 , the major contribution to its decay final state is two resolved photons. Nevertheless, both CC-RES and CC-DIS can produce pion in the final state to have some overlap with each other. But it is still possible to partially distinguish CC-RES CC-DIS events by the number of pions. Our simulation shows that for the neutrino (anti-neutrino) mode at the peak energy of 2.5 GeV, only 15% (11%) of the CC-RES events have multiple pions, while CC-DIS reaches 64% (48%). Hence the CC single-pion event can be categorized as CC-RES while the multi-pion one as CC-DIS.

The energy reconstruction formula (7) for CC-QES can no longer apply due to different particles in the final state. Instead of having nucleons in the initial and final states, CC-RES has heavy Δ baryons as intermediate resonance. Most of the pions are produced from Δ decays $\Delta^{++} \rightarrow p + \pi^+$, $\Delta^+ \rightarrow p + \pi^0$, and $\Delta^- \rightarrow n + \pi^-$ [120]. Usually the proton is not energetic enough to produce a Cherenkov ring and hence cannot be uniquely identified

but only leaves some scintillation lights. Observationally, the $\nu_e/\bar{\nu}_e$ CC-RES has a primary lepton and a pion (π^0 or π^\pm). A reasonable neutrino energy reconstruction for CC-RES is [104],

$$E_\nu^{\text{rec}} = \frac{m_\Delta^2 - m_p^2 - m_\ell^2 + 2m_p E_\ell}{2(m_p - E_\ell + |\mathbf{p}_\ell| \cos \theta_\ell)}. \quad (8)$$

Comparing with (7), the final-state nucleon mass is replaced by the Δ baryon mass, $m_\Delta = 1.232$ GeV. As demonstrated with blue lines in Fig. 8, the CC-RES energy reconstruction formula (8) gives a correct peak position. However, for the high-energy scattering process, not only Δ is produced but also other resonant particles like $N(1440)$ which can also produce pion particles. So (8) cannot describe all the resonant processes exactly and gives a wider distribution than CC-QES.

Backgrounds – The beam background for the CC-RES category has three major contributions. First, the beam electron-flavor neutrinos (anti-neutrinos) of the disappearance channel $\nu_e \rightarrow \nu_e$ ($\bar{\nu}_e \rightarrow \bar{\nu}_e$) via either CC-RES or CC-DIS scatterings contributes as irreducible background with the same $1e1\pi$ final state. Being depicted as the pink regions in Fig. 10, this type of background for neutrino (left) and anti-neutrino (right) modes contribute roughly 13.9% and 14.9% of the total detected events for $\delta_D = -90^\circ$.

The second beam background comes from the muon neutrinos ν_μ interacting via CC-RES or CC-DIS to produce μ^- and π^0 in the final state. The π^0 can fake electron if one of the decay photons is soft ($E_\gamma < 30$ MeV) or the two photons are almost collinear ($\theta_{\gamma\gamma} < 17^\circ$). For the peak energy $E_\nu = 2.5$ GeV, only 7.6% (13%) of such π^0 can fake an electron. In addition, the muon needs to be misidentified as a charged pion. With both misidentification, the beam ν_μ can fake the CC-RES signal. Although the new reconstruction algorithm of fitQun [123] shows some capability of separating pion from muon at T2K using the hadronic kinks in the pion propagation [125], we assume μ^- and π^+ can not be separated to be conservative. Not to say, μ^- has an electron but π^+ has a positron in their decay products, respectively, and the e^+e^- annihilation photons from π^+ can also provide a distinguishable feature. Note that there is no beam $\bar{\nu}_\mu$ CC background for the anti-neutrino mode. This is because the π^- in the $\bar{\nu}_e$ CC-RES signal is absorbed in the detector and does not produce a delayed Michel electron which is different from the beam $\bar{\nu}_\mu$ that can decay to μ^+ and finally a Michel e^+ . For both neutrino and anti-neutrino modes, muon misidentified as electron/positron might happen together with the same π^\pm to fake the CC-RES category. But this background can be neglected since the misidentification rate is negligibly small ($< 0.05\%$) as mentioned in Sec. III B 1. The beam ν_μ CC background is shown as green region in the left panel of Fig. 10 only for the neutrino mode.

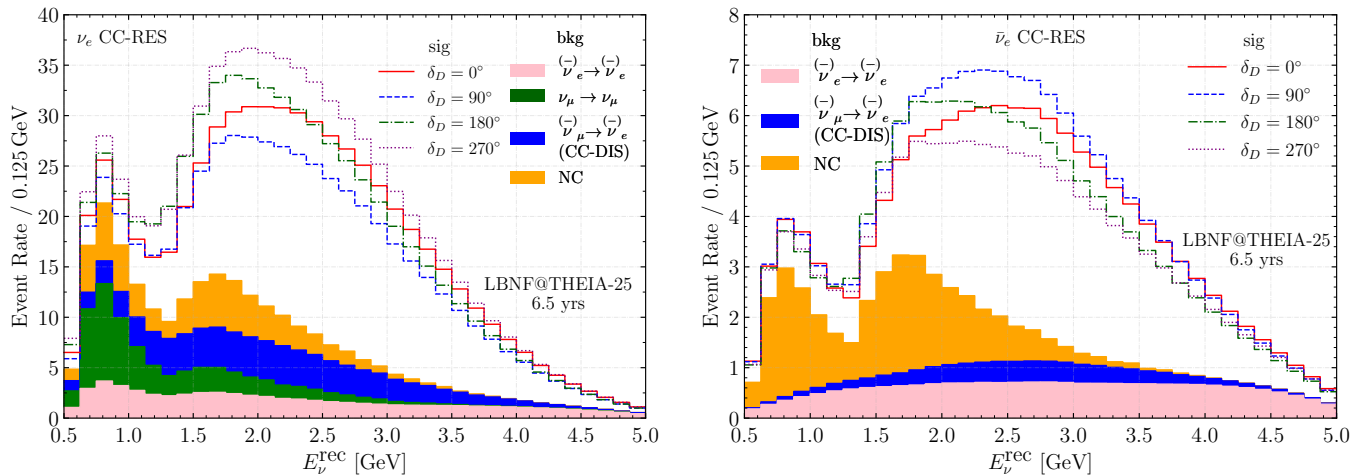


FIG. 10. The event spectra of CC-RES signal and its background at the THEIA-25 detector with LBNF neutrino (left) and anti-neutrino (right) beams. Four lines are used for $\delta_D = 0^\circ$ (solid red line), $\delta_D = 90^\circ$ (dashed blue line), $\delta_D = 180^\circ$ (dot-dashed green line) and $\delta_D = 270^\circ$ (dotted purple line). For comparison, the filled regions stand for the backgrounds of the intrinsic $\nu_e/\bar{\nu}_e$ beam CC (pink), the ν_μ CC (green), the $\nu_e/\bar{\nu}_e$ CC-DIS (blue), and NC (yellow). Both neutrino and anti-neutrino modes have 6.5 years running.

The third part of the background comes from NC-RES and NC-DIS with two pions ($2\pi^0$ or $\pi^0 + \pi^\pm$) in the final state. In such case, one π^0 decays into unresolved photons to fake the primary electron signal while the other pion coincides with the one in the signal. The estimated NC background is shown as the orange region of Fig. 10. We can see that the reconstructed NC background mostly occur at $E_\nu^{\text{rec}} < 3$ GeV.

Event Selection – In summary, the selection criteria for CC-RES signal is,

- (1) Only one primary e -like Cherenkov ring with $|p_e| > 100$ MeV.
- (2) Reconstructed neutrino energy inside the range $[0.25, 5]$ GeV.
- (3) Single pion particle in the final state. To be conservative, the events with a charged π^\pm or a neutral π^0 are not mixed into a single CC-RES category. More detailed study is necessary for maximizing the CP sensitivity.

Fig. 10 depicts the ν_e (left) and $\bar{\nu}_e$ (right) CC-RES signal and the corresponding backgrounds. Comparing the two panels, we can see that the neutrino event rates are typically 4 \sim 5 times larger than its anti-neutrino counterparts. This is a direct consequence of the relatively larger cross section for neutrino than anti-neutrino. For backgrounds, the neutrino mode has four components while the anti-neutrino mode has only three. This is because the disappearance channel $\bar{\nu}_\mu \rightarrow \bar{\nu}_\mu$ has μ^+ and Michel e^+ to be distinguished from π^- of the $\bar{\nu}_e$ CC-RES

signal. For neutrino mode, all backgrounds contribute roughly the same size while for anti-neutrino the NC and intrinsic ν_e background dominate. Around the major peak, $E_\nu^{\text{rec}} \approx 2$ GeV, the signal is slightly larger than the background for neutrino and anti-neutrino modes.

3. The CC-DIS Category

Signals – In order to enhance the statistics, we also include CC-DIS events as a separate category. As mentioned in the previous CC-RES section, the events identified as CC-DIS are those with an e -like ring accompanied with more than one pion in the final state. The majority of events contains two pions. The 2-pion events include any of the following combination (π^\pm, π^\pm), (π^\pm, π^0) and (π^0, π^0). Similar to the CC-RES category, only a pair of resolved photons are identified as π^0 . For events with one or more π^0 and consequently 3 or more e -like rings in the final state, we take the most energetic e -like ring as the primary electron/positron. Then the neutrino energy can be reconstructed using the same (8). Nevertheless, the scattering process of CC-DIS differs a lot from CC-RES and the reconstructed neutrino energy is almost flat as shown with green curves in Fig. 8.

Backgrounds – The background of the CC-DIS process also has three major contributions. The first is the irreducible one from the electron-flavor neutrinos via the CC-RES or CC-DIS with the $1eN\pi$ final state with $N > 1$. Being depicted as the pink regions in Fig. 11, this background is the largest contribution for $E_\nu^{\text{rec}} > 1.5$ GeV and can be as large as 45% of the total events at 2.5 GeV for $\delta_D = -90^\circ$.

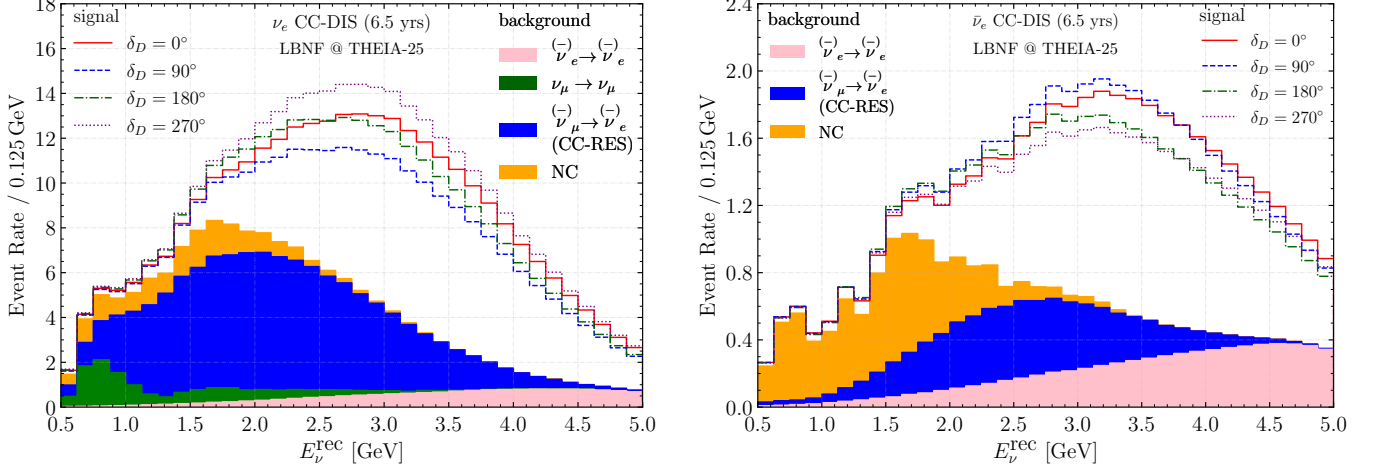


FIG. 11. The event spectra of CC-DIS signal and its background at the THEIA-25 detector with LBNF neutrino (left) and anti-neutrino (right) beams. Four solid lines are used for $\delta_D = 0^\circ$ (red), 90° (blue), 180° (green), and 270° (purple). For comparison, the filled regions stand for the backgrounds of the intrinsic $\nu_e/\bar{\nu}_e$ beam CC (pink), the ν_μ CC (green), the $\nu_e/\bar{\nu}_e$ CC-RES (blue), and the NC multi-pion events (yellow). Both neutrino and anti-neutrino modes have 6.5 years running.

The second component comes from muon neutrinos ν_μ interacting via CC-RES or CC-DIS to produce a μ^- , a π^0 and one or two other pions of any type. While μ^- is misidentified as a pion, the π^0 can be misidentified as an electron if it has a soft photon $E_\gamma < 30$ MeV or the two photons are almost collinear, $\theta_{\gamma\gamma} < 17^\circ$. The multi-pion production of two or three pions occurs for 4% of the total ν_μ CC events. In addition, the misidentification of the π^0 as an electron occurs in 17% (9%) of the events for 2-pion (3-pion) final state. This ν_μ background is shown as green curve in the left panel of Fig. 11 only for the neutrino mode. Again, there is no $\bar{\nu}_\mu$ CC background due to the delayed Michel electron veto.

The third component is the NC multi-pion background of $1\pi^0 1\pi^x 1\pi^y$ with $x, y = 0, \pm$. The triple-pion final state is reconstructed as background if one π^0 is misidentified as electron. This occurs for only 0.1% of the total NC events at the 2.5 GeV peak energy, which is represented as the orange region in Fig. 11. It is most relevant at low energies, $E_\nu^{\text{rec}} < 1.5$ GeV where the CP value has small impact.

Event Selection – We can see that the CC-DIS category has much similarity as the CC-RES one with single-pion final state replaced by the multiple one. Although the CC-DIS signal would not contribute much as shown in Fig. 8, this separation reveals the feature of various channels. Below we summarize the selection criteria for the CC-DIS signal,

- (1) Only one primary e -like Cherenkov ring with $|p_e| > 100$ MeV. In the presence of multiple e -like rings, the most energetic one is identified as the primary lepton.

- (2) Reconstructed neutrino energy inside the range $[0.25, 5]$ GeV.
- (3) At least two pions in the final state with energy $\pi(|\mathbf{p}_\pi|) > 200$ MeV. Similar to the CC-RES category, all CC-DIS events are put into a single category without division according to the final-state pions. This conservative treatment can be further improved with more careful studies.

The CC-DIS signals and their backgrounds are shown in Fig. 11. Different from the CC-QES in Fig. 9 and CC-RES in Fig. 10, the CC-DIS signal can be smaller than the background, especially for the neutrino mode. Around the peak, $E_\nu^{\text{res}} \approx 2.5$ GeV, the dominant background comes from the CC-RES multi pion background which can reach more than 50% of the total events at $E_\nu^{\text{rec}} \approx 2$ GeV. The anti-neutrino case is slightly better with signal still dominating around the peak energy. In addition, the three background components for the $\bar{\nu}_e$ mode all have sizable contributions. The NC background dominates for $E_\nu^{\text{rec}} < 2$ GeV, while the CC-RES dominates at intermediate energies $2 \text{ GeV} < E_\nu^{\text{rec}} < 3.5 \text{ GeV}$ and the intrinsic ν_e dominates for $E_\nu^{\text{rec}} > 3.5$ GeV. Nevertheless, ν_e events are 7 times larger than $\bar{\nu}_e$.

IV. CP SENSITIVITY WITH μ THEIA AND DUNE

As discussed in Sec. II, the combination of μ THEIA and DUNE is expected to improve the CP measurement. Below we give a quantitative estimation. We first summarize the experimental setups in Sec. IV A for complete-

ness and then establish the χ^2 formalism in Sec. IV B. In order to maximize the CP sensitivity, Sec. IV C explores the optimal baseline between the μ DAR source and the THEIA detector for μ THEIA. Based on these, the CP sensitivity and the influence of matter effect are studied in Sec. IV D.

A. Experimental Setups

The μ DAR neutrinos are typically produced by cyclotrons [126]. We adopt the configuration that the μ DAR flux is generated by a 9 mA proton beam with 800 MeV protons hitting the high- Z target to deliver 1.83×10^{25} POT in 10 years [87]. Since the μ DAR cyclotron is not a pulsed beam, it is possible to achieve almost full duty factor. Of the charged pions produced by proton hitting the target, π^- is mainly absorbed by the positively charged nuclei while π^+ first loses energy in the thick material and then decays at rest to produce μ^+ . Similar process of decay at rest also happens for μ^+ . Consequently, the μ DAR neutrino spectra are well defined and predicted by the SM interactions.

For DUNE, the LBNF neutrinos are produced by 120 GeV protons with 1.2 MW beam power and the flux can reach 1.1×10^{21} POT/year. We take 6.5 years running for each neutrino and anti-neutrino mode [44]. With completely different energy windows [30, 55] MeV for μ DAR and [0.5, 5] GeV for LBNF, there is no energy overlap between the low-energy μ DAR flux and the high-energy LBNF one. So the two fluxes can run simultaneously.

For the THEIA detector we consider two possibilities, THEIA-25 with a fiducial mass of 17 kt and THEIA-100 with a fiducial mass of 70 kt [51]. The DUNE detector has four modules, each with 10 kt fiducial mass [122]. Both THEIA and DUNE detectors are at the same SURF site and 1289 km away from the LBNF source. To install the THEIA detector, one of the DUNE modules needs to be replaced. As mentioned in Sec. II, the average matter density 2.85 g/cm^3 is used for both DUNE and μ THEIA.

In the following, we consider three combinations: (1) the full DUNE configuration with 4 far detector modules, (2) the reduced DUNE with 3 far detector modules and μ THEIA-25, and (3) the reduced DUNE and μ THEIA-100. The high-energy mode (HEM) can be detected by both the DUNE and THEIA detectors while the low-energy mode (LEM) only applies for the THEIA detector as discussed in Sec. III. The energy window, fiducial mass, baseline, and running time of each experimental configurations are summarized in Tab. I.

B. Simulation and χ^2 Analysis

We then use GLoBES [127, 128] to simulate the event rates and evaluate the CP sensitivities. A quantitative

evaluation is realized by minimizing the χ^2 function that

	DUNE (HEM)	DUNE + μ THEIA-25/100 (HEM)	μ THEIA-25/100 (LEM)
Energy Window (GeV)	[0.5, 5]	[0.5, 5]	[0.03, 0.055]
Fiducial Mass (kt)	40	30+17/70	17/70
Running Time (ν y, $\bar{\nu}$ y)	(6.5, 6.5)	(6.5, 6.5)	(0, 10)
Baseline (km)	1289	1289	??
Density (g/cm^3)	2.85	2.85	2.85

TABLE I. The energy window, fiducial mass, running time, baseline, and matter density for the three experimental setups considered in this paper.

contains three contributions,

$$\chi^2 \equiv \chi_{\text{stat}}^2 + \chi_{\text{sys}}^2 + \chi_{\text{para}}^2, \quad (9)$$

for statistical (χ_{stat}^2) and systematical (χ_{sys}^2) uncertainties in addition to the prior constraint on the oscillation parameters (χ_{para}^2).

For event rate > 10 in a single bin, a Gaussian χ^2 is much more convenient with analytical fit [100, 129, 130]. However, the event rates considered in this paper are not large enough. To make the sensitivity evaluation exact, the statistical part in the first term takes the Poisson form,

$$\chi_{\text{stat}}^2 \equiv 2 \sum_{\text{bins}} \left[(1 + a_{\text{sig}}) N_i^{\text{sig}} + (1 + a_{\text{bkg}}) N_i^{\text{bkg}} - N_i^{\text{data}} - N_i^{\text{data}} \ln \left(\frac{(1 + a_{\text{sig}}) N_i^{\text{sig}} + (1 + a_{\text{bkg}}) N_i^{\text{bkg}}}{N_i^{\text{data}}} \right) \right], \quad (10)$$

where N_i^{data} , N_i^{sig} and N_i^{bkg} are the pseudo data, signal and background event numbers in the i -th bin, respectively. The coefficients a_{sig} and a_{bkg} are nuisance parameters for the signal and background normalizations, respectively.

The χ_{sys}^2 term contains the uncorrelated Gaussian priors of signal and background normalizations. We take $\sigma_{\text{sig}} = 5\%$ and $\sigma_{\text{bkg}} = 10\%$ for each channel of both the low- and high-energy modes that are observed at the THEIA detector. For the low-energy mode, the normalization uncertainties are the same as the configuration given in [87] while the uncertainties are more conservative than the values (2% for ν_e and 5% for $\bar{\nu}_e$) used in [51]. The systematics of the LBNF beam detection by the DUNE detector are described by the official configuration files [122].

Finally, χ_{para}^2 contains the prior information on the oscillation parameters. Their best fit values are obtained

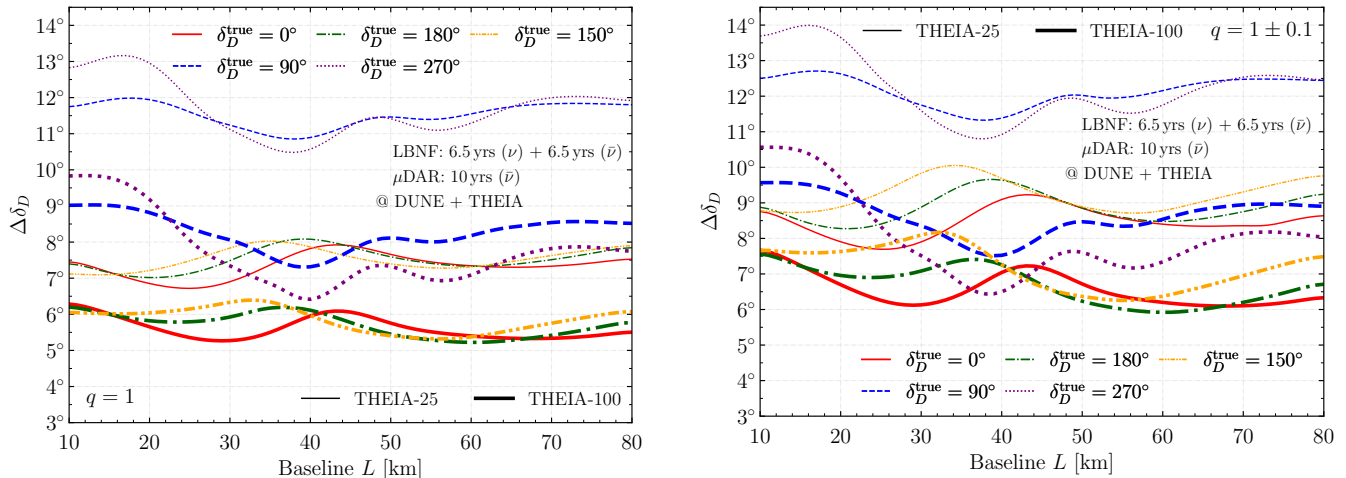


FIG. 12. The CP phase uncertainty, $\Delta\delta_D$, for the combination of DUNE and THEIA as a function of the μ THEIA baseline L for true values $\delta_D^{\text{true}} = 0^\circ$ (red), 90° (blue), 180° (green), 270° (purple), and 150° (orange). While the LBNF flux runs for 6.5 years each in the neutrino and anti-neutrino modes, μ DAR provides 10 years for the anti-neutrino mode. The larger DUNE + μ THEIA-100 (thick lines) has much smaller CP uncertainty than DUNE + μ THEIA-25 (thin lines). To illustrate the matter effect on the CP uncertainty, simulations with fixed $q = 1$ and a 10% prior on q are shown in the left and right panels, respectively.

from the global fit result [131],

$$\sin^2 \theta_s = 0.318, \quad \sin^2 \theta_a = 0.574, \quad \sin^2 \theta_r = 0.022, \quad (11a)$$

$$\Delta m_s^2 = 7.50 \times 10^{-5} \text{ eV}^2, \quad \Delta m_a^2 = 2.55 \times 10^{-3} \text{ eV}^2, \quad (11b)$$

where we take NO in our study.

Among these oscillation parameters, the solar mass squared difference Δm_s^2 and the solar mixing angle θ_s are kept fixed throughout our analysis. On one hand, the contribution of the solar mass squared difference Δm_s^2 enters via a coefficient parameter $\alpha \equiv \Delta m_s^2 / \Delta m_a^2$ as shown in (3). The parameter α has a small value (≈ 0.03) and the error in Δm_s^2 has an even smaller contribution. Hence it can be neglected comparing with the $\mathcal{O}(1)$ uncertainty on the CP phase. On the other hand, the solar mixing angle appears in the first and the third term on the right-hand side of (3). Since the current prior on the solar mixing angle is roughly 3%, it can also be neglected for the study of the large CP phase uncertainty. Moreover, the next generation reactor neutrino experiment like JUNO [63] will provide a sub-percent uncertainty on θ_s that is negligibly small.

For the other mixing parameters, the reactor mixing angle θ_r , the atmospheric mixing angle θ_a , and the atmospheric mass-square difference Δm_a^2 are treated as free parameters. We use the marginalized one-dimensional χ^2 curves [131] as our priors, $\chi_{\text{para}}^2 \equiv \chi_{\theta_r}^2 + \chi_{\theta_a}^2 + \chi_{\Delta m_a^2}^2$. Due to the existing tension between the T2K and NO ν A results, which is discussed in Sec. I, we do not include any prior on δ_D .

Since the matter effect is a natural source of fake CP, we take its uncertainty by including a parameter q to scale its average value defined in Sec. II, $A \rightarrow qA$ [132].

The average matter density corresponds to $q = 1$ while the vacuum case takes $q = 0$. Note that q is undetermined and hence treated as the fifth free parameter. In the following discussions, we consider two different scenarios for its uncertainty: fixed $q = 1$ (no uncertainty) and a conservative 10% Gaussian uncertainty. For comparison, previous studies have used 1% \sim 2% uncertainty [45, 133–135].

The CP uncertainty $\Delta\delta_D$ is defined as the half-width of the $\Delta\chi^2 = \chi^2(\delta_D) - \chi_{\text{min}}^2 = 1$ band where χ_{min}^2 corresponds to the best-fit value δ_D^{BF} of the CP phase. Since our simulation uses pseudo-data, the best-fit value is the same as the true value, δ_D^{true} . Note that it is not necessary for the $\chi^2(\delta_D)$ function to be symmetric around the minimum. For this case, the previous definition, $\Delta\chi^2 = 1$, gives two boundaries below (δ_D^-) and above (δ_D^+) the best-fit value δ_D^{BF} . Then we take the average deviation as the CP uncertainty, $\Delta\delta_D \equiv (\delta_D^+ - \delta_D^-)/2$.

C. Baseline Options of μ THEIA

The baseline between the μ DAR source and the THEIA detector can significantly affect the CP uncertainty $\Delta\delta_D$. Fig. 12 shows $\Delta\delta_D$ as a function of the μ THEIA baseline L in the range from 10 km to 80 km. Since the true value of the CP phase δ_D^{true} is unknown, it needs to be varied. Four typical CP values $\delta_D^{\text{true}} = 0^\circ, 90^\circ, 180^\circ$ and 270° are chosen for illustration. In addition, $\delta_D^{\text{true}} = 150^\circ$ is not only preferred by the current result of NO ν A but also significantly affected by the matter effect uncertainty as elaborated in Sec. IV D.

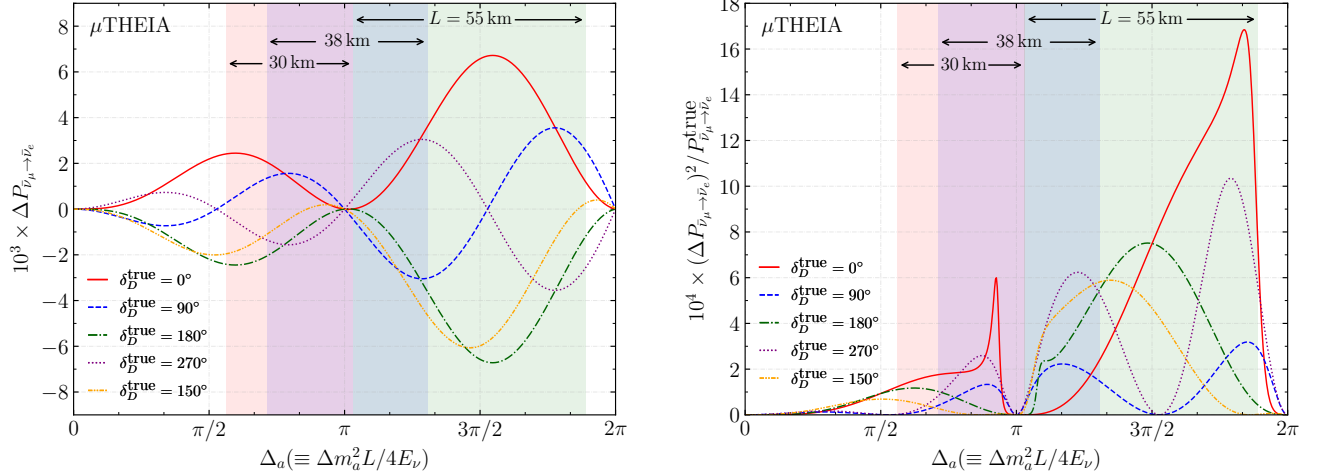


FIG. 13. **Left:** The oscillation probability difference $\Delta P_{\bar{\nu}_\mu \rightarrow \bar{\nu}_e}$ between the true (δ_D^{true}) and fitting (δ_D^{fit}) CP values as a function of the atmospheric oscillation phase $\Delta_a \equiv \Delta m_a^2 L/4E_\nu$. Five different true CP values $\delta_D^{\text{true}} = 0^\circ$ (red), 90° (blue), 180° (green), 270° (purple), and 150° (orange) are shown for comparison. The fitting values δ_D^{fit} are assigned 10° larger than the corresponding δ_D^{true} values. The neutrino energy varies within $[30, 55]$ MeV while the baseline is fixed at three different baselines, $L = 30$ km (red region), 38 km (purple region), and 55 km (light green region). **Right:** The relative difference $(\Delta P_{\bar{\nu}_\mu \rightarrow \bar{\nu}_e})^2 / P_{\bar{\nu}_\mu \rightarrow \bar{\nu}_e}^{\text{true}}$ with the same setups.

So we also show the $\delta_D^{\text{true}} = 150^\circ$ curve for comparison. Both THEIA-25 (thin lines) and THEIA-100 (thick lines) are considered. With larger detector size, the CP uncertainty decreases but the baseline dependence follows the same trend.

To see the impact of matter effect on the optimal baseline, the left panel of Fig. 12 is obtained by fixing $q = 1$ while the right one takes $q = 1 \pm 0.1$. For both cases, the result shows two local minima in the CP uncertainty for maximal CP violation. One is around $L = 38$ km and the other around $L = 55$ km. The longer one, $L = 55$ km, is a local optimal option for $\delta_D = 270^\circ$ that is preferred by the T2K measurement. Although the true local minimum for vanishing CP violation cases $\delta_D = 0^\circ$ and 180° actually happens with $L \gtrsim 65$ km, the difference in χ^2 is not significant while the maximal CP violation cases $\delta_D = 90^\circ$ and 270° (or equivalently -90°) become much worse. Since the data-driven $\delta_D = -90^\circ$ is of larger interest, $L = 55$ km is preferred than the longer 65 km. For the shorter one, the choice is more difficult. The global minimum around $L \approx 38$ km for $\delta_D = \pm 90^\circ$ is very close to the global maximum for the vanishing CP violation cases. So choosing $L = 38$ km needs to pay too much price and we take $L = 30$ km to balance among various CP values. Our simulations takes these three baselines $L = 30$ km, 38 km, and 55 km as possible options. The final choice is up to the on-going T2K and NO ν A experiments. The comparison between the left (fixed $q = 1$) and right (10% uncertainty around $q = 1$) panels of Fig. 12 shows that although the uncertain matter effect contaminates the CP sensitivity, increasing $\Delta\delta_D$ by 3 or 4 degrees to be exact, it does not affect the optimal baselines.

The optimal baseline options $L = (30, 38, 55)$ km for DUNE + μ THEIA are all different from the TNT2HK one $L = 23$ km [87]. Not just the baseline length is different, but also TNT2K/TNT2HK obtains only a single local minimum. The key difference is the atmospheric invisible muon background. Since both SK and HK are water Cherenkov detectors, the atmospheric invisible muon dominates the background. As L increases, the beam flux decreases with $1/L^2$, but the atmospheric background remains the same and eventually dominates the statistics. So the relatively large amount of the atmospheric background limits the optimal baseline length. For comparison, THEIA with WbLS reduces the invisible muons to negligible amount as shown in Fig. 7. Therefore, μ THEIA can have longer baseline than TNT2K/TNT2HK to optimize the CP sensitivity.

While the options $L = 30$ km and 38 km are not so far from the 23 km of TNT2K/TNT2HK and hence easier to understand, the longer baseline $L = 55$ km also achieving comparable CP sensitivities seems counter-intuitive. From 30 km to 55 km, the flux decreases quadratically with distance and is suppressed by a factor $(30/55)^2 \approx 0.3$. However, this flux reduction is compensated by the increasing oscillation amplitude. To make this feature explicit, we show in the left panel of Fig. 13 the oscillation probability difference, $\Delta P_{\bar{\nu}_\mu \rightarrow \bar{\nu}_e} (\equiv P_{\bar{\nu}_\mu \rightarrow \bar{\nu}_e}^{\text{fit}} - P_{\bar{\nu}_\mu \rightarrow \bar{\nu}_e}^{\text{true}})$, between the true (δ_D^{true}) and fit (δ_D^{fit}) CP values,

$$\begin{aligned} \Delta P_{\bar{\nu}_\mu \rightarrow \bar{\nu}_e} &= 16\Delta_s s_r c_s s_s c_a s_a \sin \Delta_a \\ &\times \sin \frac{\Delta' \delta_D}{2} \sin \left(\frac{2\Delta_a - 2\delta_D^{\text{true}} - \Delta' \delta_D}{2} \right). \end{aligned} \quad (12)$$

Note that this formula is obtained from (3) in the vac-

uum limit ($A \rightarrow 0$). The oscillation and CP phases are defined as $\Delta_{a,s} \equiv \Delta m_{a,s}^2 L/4E$ and $\Delta' \delta_D \equiv \delta_D^{\text{fit}} - \delta_D^{\text{true}}$. To further illustrate the CP sensitivity, the parameter $(\Delta P_{\bar{\nu}_\mu \rightarrow \bar{\nu}_e})^2 / P_{\bar{\nu}_\mu \rightarrow \bar{\nu}_e}^{\text{true}}$ that has a similar form as the χ^2 calculation is also calculated in the right panel of Fig. 13. For convenience, we name $(\Delta P)^2 / P$ as *pseudo- χ^2* at the oscillation probability level. Both variables are shown as a function of the atmospheric oscillation phase Δ_a ($\equiv \Delta m_a^2 L/4E_\nu$) for five different true CP values, $\delta_D^{\text{true}} = 0^\circ, 90^\circ, 180^\circ, 270^\circ$, and 150° . The difference between the fitting and true CP values are assigned to have $\Delta' \delta_D = 10^\circ$ for illustration.

The left panel shows that the second peak of the oscillation probability difference ΔP is much larger than the first one and the relative size between the pseudo- χ^2 peaks in the right panel is also significantly enhanced. Take the $\delta_D^{\text{true}} = 0^\circ$ curve in the right panel as an example, the second peak is 3 times of the first one which can roughly compensate the flux suppression (~ 0.3). Similar feature applies also for the other true CP values. This explains why the local minimum around $L = 55$ km has roughly the same value at $L = 30$ km.

The three filled regions correspond to different baselines $L = 30$ km, 38 km, and 55 km, respectively, while the μDAR neutrino energy E_ν spans a wide range of $[30, 55]$ MeV. With Δ_a inversely proportional to E_ν , the left boundary of each region corresponds to the upper energy limit 55 MeV and the right one to the lower limit 30 MeV. Since the $\bar{\nu}_\mu$ spectrum from μDAR source peaks at the upper limit [87], the left sides of the filled regions give the largest contribution. This important feature can explain the location of those local minimums in Fig. 12. For example, the left side of the pink region for $L = 30$ km covering the first oscillation peak/valley of $\delta_D^{\text{true}} = 0^\circ$ in Fig. 13 explains why this baseline corresponds to the best sensitivity of this true CP value in Fig. 12. The same thing happens for $L = 38$ km with the left side of the purple region covering the $\delta_D^{\text{true}} = \pm 90^\circ$ peak/valley in Fig. 13 to justify the local minimum in Fig. 12. Not to say the left side of the light green region of $L = 55$ km covers the second peak/valley of $\delta_D^{\text{true}} = \pm 90^\circ$ in Fig. 13.

D. CP Sensitivity and Matter Effect

As emphasized in earlier discussions, the CP sensitivity suffers from matter effect contamination. The DUNE + μTIEIA configuration we propose in this paper can overcome this issue to provide a clean measurement of the Dirac CP phase δ_D . Fig. 14 shows the CP uncertainty $\Delta\delta_D$ as a function of the true value δ_D^{true} for three μTIEIA benchmark baselines, $L = 30$ km (top), 38 km (middle), and 55 km (bottom) found in the previous Sec. IV C. For each baseline, we consider several scenarios: 1) DUNE alone with 4 modules, DUNE with 3 modules and 2) $\mu\text{TIEIA-25}$ or 3) $\mu\text{TIEIA-100}$. More details are summarized in Tab. I.

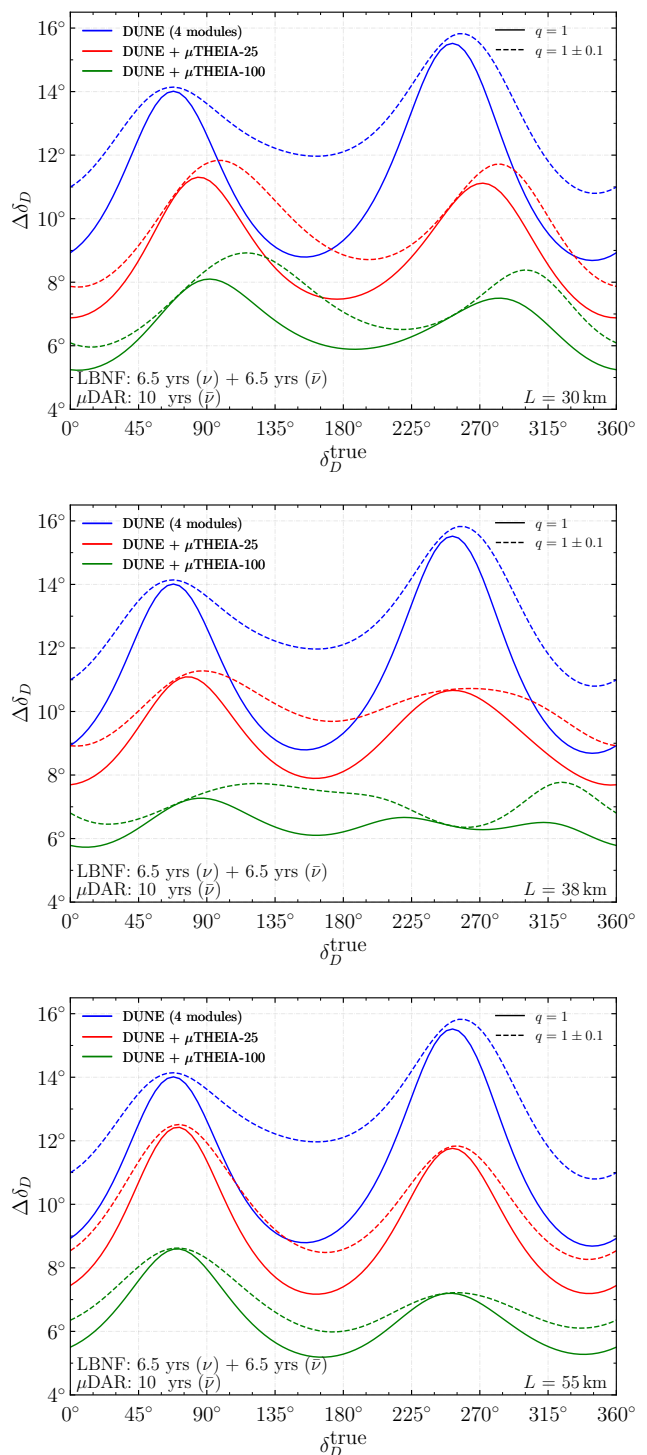


FIG. 14. The CP phase uncertainty $\Delta\delta_D$ as a function of the true CP value δ_D^{true} . For illustration, the three μTIEIA baseline options $L = 30$ km (top), 38 km (middle), and 55 km (bottom) are shown separately. Each panel takes three different experimental setups, DUNE with 4 modules (blue), DUNE with 3 modules and $\mu\text{TIEIA-25}$ (red) or $\mu\text{TIEIA-100}$ (green). As for the matter effect, both the fixed case ($q = 1$, solid) and 10% uncertainty ($q = 1 \pm 0.1$, dashed) are implemented to show how it affects the CP sensitivity.

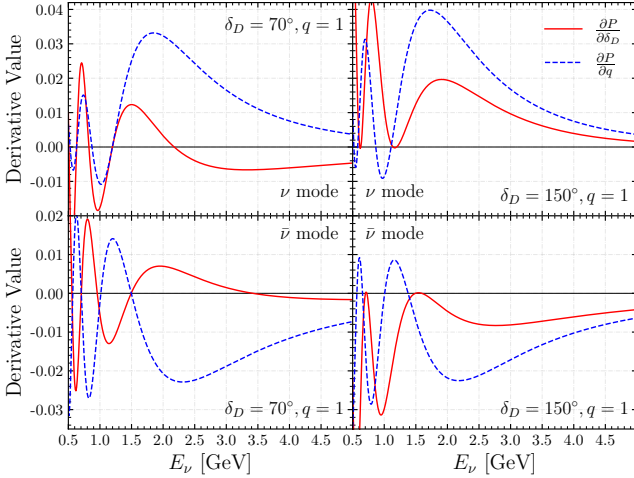


FIG. 15. Oscillation probability derivatives $\partial P/\partial\delta_D$ (red solid) and $\partial P/\partial q$ (blue dashed) with respect to the matter effect parameter q at $q = 1$ and the Dirac CP phase δ_D , respectively. Both neutrino and anti-neutrino modes are shown in the upper and lower rows for comparison. The left column adopts $\delta_D = 70^\circ$ while the right one takes $\delta_D = 150^\circ$.

In all panels, the DUNE configuration contains the full 40kt detector and the blue curves do not change with varying L since it does not depend on μ THEIA baseline. For fixed matter effect ($q = 1$), the CP uncertainty peaks around $\delta_D^{\text{true}} \approx 70^\circ$ and 250° which are consistent with [65, 133, 135, 136] where either fixed matter effect or just 2% uncertainty is adopted. Slightly shifted peaks at $\delta_D^{\text{true}} \approx 90^\circ$ and 270° are obtained and attributed to different treatment of systematics in [137].

From DUNE alone to DUNE + μ THEIA-25, the CP uncertainty $\Delta\delta_D$ significantly reduces by roughly 1/4. This is especially true around the maximal CP values, $\delta_D^{\text{true}} = \pm 90^\circ$ since the μ DAR spectrum is especially wide to provide both $\cos\delta_D$ and $\sin\delta_D$ terms. With only $\sin\delta_D$ term, the CP uncertainty around the maximal CP phase is intrinsically large, $\Delta\delta_D \propto 1/\cos\delta_D$. But a wide spectrum can also introduce a large enough $\cos\delta_D$ term to make the CP uncertainty decrease. Previous study shows that this feature is expected to appear when μ DAR flux is added to supplement the narrow beam accelerator experiments, such as TNT2K/TNT2HK [40–42, 87]. Nevertheless, the result turns out that this is also true for the addition of μ THEIA to DUNE, although the LBNF flux spectrum is already quite wide. Adding a larger μ THEIA-100 can even further reduce the CP uncertainty to almost only 5° for the best case.

As expected, the matter effect can fake the CP violation and hence its uncertainty can significantly modify the CP uncertainty. In addition to the fixed $q = 1$ scheme (solid lines), Fig. 14 also shows the results obtained with 10% uncertainty in the matter effect or equivalently $q = 1 \pm 0.1$ (dashed lines). With q relaxed, the CP uncertainty becomes much worse especially around the vanishing CP violation, $\delta_D^{\text{true}} \approx 0^\circ$ or 180° . The

most significantly affected point is around $\delta_D^{\text{true}} \approx 150^\circ$ or 330° . With the uncertainty of matter effect taken into account, the improvement brought by μ THEIA is even more significant. This is exactly because of the fact that matter effect plays more important role at DUNE with much higher energy than the low-energy μ THEIA. With μ THEIA added, even switching on matter effect uncertainty would not make the situation much worse. It also is interesting to see that the CP uncertainty around the maximal CP violation is almost not affected by switching on/off the matter effect uncertainty. The μ THEIA improvement is quite stable against matter effect.

To understand the interplay between the Dirac CP phase and the matter effect qualitatively, Fig. 15 shows the partial derivative $\partial P/\partial\delta_D$ of oscillation probability (3) with respect to the Dirac CP phase δ_D and $\partial P/\partial q$ to the matter effect parameter q at $q = 1$ as a function of neutrino energy E_ν . The matter effect mimics the CP effect quite well at $\delta_D^{\text{true}} = 150^\circ$ with the two derivative curves having similar shapes and peak positions. For comparison, the two derivatives have very different features at 70° .

Note that the green curves with DUNE and μ THEIA-100 are much more flat than the original DUNE alone. For most of the parameter space, the CP uncertainty is better than 8° . Among the three panels of Fig. 14, the $L = 38$ km one has the most flat CP uncertainty curves for the DUNE + μ THEIA-100 configuration. Especially, the CP certainty is always better than 8° no matter what is the value of δ_D^{true} . In this sense, $L = 38$ km is probably the optimal baseline for μ THEIA.

To further illustrate the advantages of the DUNE + μ THEIA combination, we compare with other existing experiments or designs in Fig. 16. The first two rows show the latest measurements from the NO ν A ($\delta_D = 148^\circ_{-157^\circ}^{+49^\circ}$) [25] and T2K ($\delta_D = -108^\circ_{-33^\circ}^{+40^\circ}$) [24]. The T2K experiment has two major upgrades: T2HK [43] with a much larger Hyper-K detector and T2HKK [56] with another detector at the second oscillation peak. For both of them, a matter effect uncertainty of 6% is considered [56]. Since T2HK is in construction and T2HKK still being planned, there is no real data yet. We take two typical values $\delta_D = -90^\circ$ and 150° for illustration. At these two true values, the CP uncertainty at T2HK (T2HKK) can reach $22^\circ(13^\circ)$ and $10^\circ(7^\circ)$, respectively [43, 56].

The experiments listed in Fig. 16 are sorted according to their CP uncertainties. After T2K and their upgrades, the next one is the DAE δ ALUS experiment that uses μ DAR neutrinos. With three cyclotrons, its CP uncertainty touches down to 18° (28°) at the chosen typical CP phase $\delta_D = -90^\circ$ (150°) [84]. Another μ DAR experiment design [85] uses the JUNO detector [63]. The combination of DAE δ ALUS + JUNO can achieve even better sensitivity than DAE δ ALUS alone with an uncertainty of 18° (21°) at $\delta_D = -90^\circ$ (150°) [86].

The next group is the accelerator-based DUNE [44] and MOMENT [59]. The CP uncertainty at DUNE is

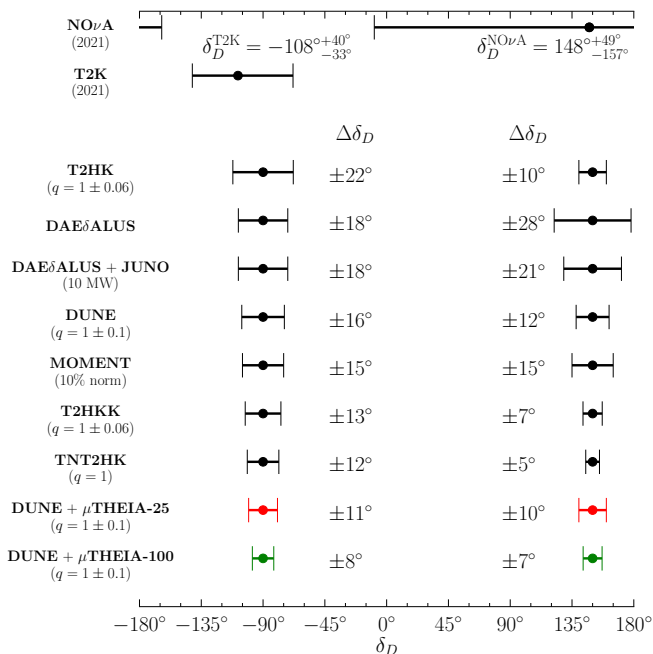


FIG. 16. The current δ_D measurement at T2K and NO ν A. For comparison, the projected CP sensitivities at various future and planned experiments are sorted by the size of CP uncertainty. For T2K and NO ν A that are already running, their latest results from real experimental data are shown while for those still in plan or design, we simply quote the CP uncertainty at two typical CP phase values $\delta_D = -90^\circ$ and 150° for illustration. These experiments are sorted according to their uncertainties around $\delta_D = -90^\circ$.

derived from our own simulation with a conservative 10% uncertainty in the matter potential, as shown in Fig. 14. Different from the μ DAR flux, the neutrino flux from muon decay in flight is adopted by the MOMENT experiment to 15° [138].

Finally, TNT2HK and the two DUNE+ μ THEIA-25/100 configurations use μ DAR neutrinos to supplement the accelerator measurements. Since the Hyper-K detector is going to be built, TNT2HK will always dominate over TNT2K once a μ DAR source is added around the Kamioka site. So we only show TNT2HK in Fig. 16. Among these three options, TNT2HK has the advantage of using the full Hyper-K detector including Super-K for the detection of both the accelerator and μ DAR neutrinos. Nevertheless, the atmospheric invisible muon background limits its CP uncertainty to 12° at regions around maximum CP phase. [87]. In addition, the J-PARC beam energy and flux [20] are also lower than the LBNF ones [44]. Although the μ THEIA-25 can only use a fiducial volume of 17 kt, the CP uncertainty 11° (10°) at DUNE + μ THEIA-25 is already slightly better than TNT2HK. With 70 kt fiducial volume at μ THEIA-100, the CP uncertainty further reduces to only $7^\circ \sim 8^\circ$. This clearly shows the advantages of supplementing DUNE with μ THEIA-25 or μ THEIA-100.

V. CONCLUSION AND OUTLOOK

The leptonic CP phase measurement at accelerator-based neutrino oscillation experiments suffers from the contamination of matter effect. The higher neutrino energy, the more severe contamination. In this paper, we put forward a possible combination of intrinsically low-energy μ DAR neutrinos and the recently proposed THEIA detector to overcome this problem.

Our simulation shows that the THEIA detector using WbLS has very good capability of particle identification. This is especially useful for suppressing the atmospheric invisible muon background, which was the major background at the TNT2K/TNT2HK configuration, to negligible amount. Then the μ DAR $\bar{\nu}_\mu \rightarrow \bar{\nu}_e$ oscillation leaves a very clear IBD signal in the detector. In addition, the high-energy LBNF flux can also be measured at the THEIA detector in addition to DUNE.

With essentially a background free measurement, the enhancement on CP sensitivity from μ THEIA is significant. The CP uncertainty around the maximal CP violation $\delta_D = \pm 90^\circ$ reduces up to 20% (40%) when compared to the standard DUNE configuration. Especially, the CP uncertainty is controlled to be below 8° and the best case can be as good as 6° for the baseline $L = 38$ km. In addition, the dependence of CP uncertainty on the true CP phase value is largely mitigated. If realized, either the DUNE + μ THEIA-25 or DUNE + μ THEIA-100 configuration can bring the CP measurement into a precision era.

ACKNOWLEDGEMENTS

The authors are grateful to Constantinos Andreopoulos, Junting Huang, Robert Svoboda, Julia Tena Vidal, Zhe Wang, and Guang Yang for valuable discussions and helps. The authors are supported by the Double First Class start-up fund (WF220442604) provided by Tsung-Dao Lee Institute & Shanghai Jiao Tong University, the Shanghai Pujiang Program (20PJ1407800), and National Natural Science Foundation of China (No. 12090064). This work is also supported in part by Chinese Academy of Sciences Center for Excellence in Particle Physics (CCEPP).

Appendix A: The Wrong Scattering Angle Effect

As demonstrated in Sec. III A 1, a more precise energy reconstruction for the IBD signal requires both momentum and the scattering angle θ_e in (5). Reconstructing the scattering angle is possible for the μ DAR neutrinos with fixed source location. Unfortunately, the direction of the incoming atmospheric neutrino is unknown. So the atmospheric neutrino background suffers from the *wrong scattering angle effect* which can further blur the neutrino energy reconstruction.

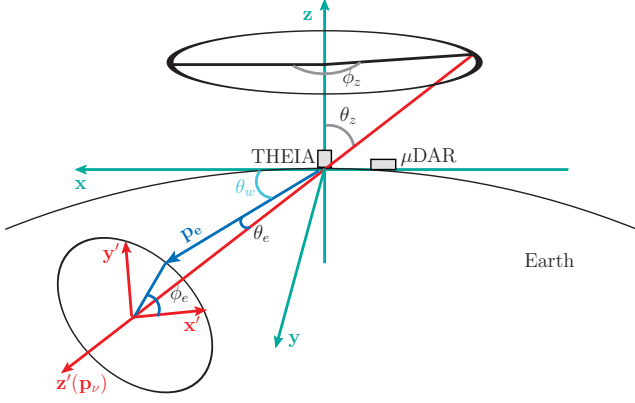


FIG. 17. The schematic show of the wrong scattering angle effect for the measurement of atmospheric neutrinos. During the scattering process, the incoming neutrino with momentum \mathbf{p}_ν (long red arrow) becomes an electron/positron with momentum \mathbf{p}_e (blue arrow). The neutrino momentum ($-\mathbf{p}_\nu$) is parameterized by θ_z and ϕ_z in the lab frame (green) while the electron/positron momentum (\mathbf{p}_e) by θ_e and ϕ_e in the neutrino frame. Without knowing the incoming neutrino direction, the genuine scattering angle θ_e is wrongly reconstructed as θ_w .

Fig. 17 shows the geometry of the atmospheric IBD background. With $\mathcal{O}(10)$ km baseline, the μ DAR neutrinos essentially travels horizontally, providing a natural definition of the x -axis while the other horizontal direction is the y -axis of the lab frame (cyan). Then, the zenith angle θ_z is measured from the vertical z -axis. Given θ_z , the incoming atmospheric neutrino direction is parametrized by the azimuth angle ϕ_z , measured from the x -axis. The final-state lepton typically has a nonzero scattering angle θ_e from the neutrino direction. For convenience, a neutrino frame (blue) is established around the neutrino momentum \mathbf{p}_ν with x' , y' , and z' -axes.

The wrong scattering angle is defined as the one between the direction of e^-/e^+ (blue arrow) and the direction of the μ DAR flux (cyan x -axis). For comparison, the true scattering angle θ_e and the corresponding azimuth angle ϕ_e are also plotted in the figure. To calculate the wrong angle as a function of θ_e , θ_z , ϕ_e , and ϕ_z , one need to first establish the connection between the horizontal and neutrino frames. The z' direction can be easily read out from the figure, $\vec{z}' = -\sin\theta_z \cos\phi_z \vec{x} - \sin\theta_z \sin\phi_z \vec{y} - \cos\theta_z \vec{z}$. But the x' - and y' -axes can be randomly set, as long as they satisfy $\vec{n}_{x'} \cdot \vec{n}_{z'} = \vec{n}_{y'} \cdot \vec{n}_{z'} = \vec{n}_{x'} \cdot \vec{n}_{y'} = 0$, $|\vec{n}_{x'}| = |\vec{n}_{y'}| = 1$ and $\vec{n}_{x'} \times \vec{n}_{y'} = \vec{n}_{z'}$. Accordingly, the following transform-

ation matrix between two coordinate systems is chosen,

$$\begin{pmatrix} \vec{x}' \\ \vec{y}' \\ \vec{z}' \end{pmatrix} = \begin{pmatrix} -\cos\theta_z \cos\phi_z & -\cos\theta_z \sin\phi_z & \sin\theta_z \\ -\sin\phi_z & \cos\phi_z & 0 \\ -\sin\theta_z \cos\phi_z & -\sin\theta_z \sin\phi_z & -\cos\theta_z \end{pmatrix} \begin{pmatrix} \vec{x} \\ \vec{y} \\ \vec{z} \end{pmatrix}. \quad (\text{A1})$$

The e^-/e^+ direction in the neutrino frame is $(\sin\theta_e \cos\phi_e, \sin\theta_e \sin\phi_e, \cos\theta_e)$. Using the frame transformation (A1), the e^-/e^+ direction in the lab frame is

$$\vec{n}_e = \begin{pmatrix} -c_z^\phi s_z^\theta c_e^\theta - s_e^\theta (c_z^\phi c_e^\phi c_z^\phi + s_e^\phi s_z^\phi) \\ -s_z^\phi s_z^\theta c_e^\theta + s_e^\theta (-c_z^\phi c_e^\phi s_z^\phi + c_z^\phi s_e^\phi) \\ -c_z^\theta c_e^\theta + c_e^\phi s_z^\theta s_e^\theta \end{pmatrix}^T, \quad (\text{A2})$$

where we have used shorthand notations, $(c_{e,z}^\phi, s_{e,z}^\phi) \equiv (\cos\phi_{e,z}, \sin\phi_{e,z})$ and $(c_{e,z}^\theta, s_{e,z}^\theta) \equiv (\cos\theta_{e,z}, \sin\theta_{e,z})$.

With μ DAR flux in the direction of $\vec{n}_{\mu\text{DAR}} = (1, 0, 0)$, the cosine term of the wrong scattering angle θ_w is given by

$$\begin{aligned} \cos\theta_w &\equiv \vec{n}_e \cdot \vec{n}_{\mu\text{DAR}} / |\vec{n}_e| |\vec{n}_{\mu\text{DAR}}| \\ &= -\cos\phi_z \sin\theta_z \cos\theta_e \\ &\quad -\sin\theta_e (\cos\theta_z \cos\phi_e \cos\phi_z + \sin\phi_e \sin\phi_z). \end{aligned} \quad (\text{A3})$$

To see the effect of a wrong scattering angle, we use Monte Carlo method to randomly generate the scattering process. As seen from Fig. 17, there are four different angles in the whole scattering process and each of them has specific probability distribution. First, the zenith angle of the atmospheric neutrino flux θ_z is defined as the angle between the local zenith and the direction of atmospheric neutrino flux [139]. Its probability distribution is sampled according to the low energy Gran Sasso flux downloaded from the Honda website [119]. Given a zenith angle θ_z , the azimuth angle θ_e is isotropically sampled since the location of the μ DAR source is not known yet.

From the atmospheric neutrino scattering with target, the scattering angle θ_e of the final-state charged lepton distributes according to the GENIE simulation. One important feature is that the $\cos\theta_e$ distribution depends on the neutrino energy E_ν . Moreover, the lepton azimuth angle ϕ_e is isotropic.

In addition, the atmospheric neutrino flux is affected by the neutrino oscillation through the Earth which is a function of the propagation length $2R \cos\theta_z$ where $R = 6371$ km is the Earth radius. We use the PREM Earth model [140] that is implemented in GLOBES to calculate the oscillation probability to calculate the modified atmospheric neutrino flux.

As expected, the wrong scattering angle significantly affects the energy reconstruction since the scattering angle in the energy reconstruction formula (5) plays an important role as we discussed in Sec. III A 1. The reconstructed energy spectra at several different typical energies are shown in Fig. 4.

- [1] G. C. Branco, R. G. Felipe and F. R. Joaquim, “*Leptonic CP Violation*,” *Rev. Mod. Phys.* **84**, 515-565 (2012) [arXiv:1111.5332 [hep-ph]].
- [2] L. Canetti, M. Drewes and M. Shaposhnikov, “*Matter and Antimatter in the Universe*,” *New J. Phys.* **14**, 095012 (2012) [arXiv:1204.4186 [hep-ph]].
- [3] C. Balazs, “*Baryogenesis: A small review of the big picture*,” [arXiv:1411.3398 [hep-ph]].
- [4] B. Garbrecht, “*Why is there more matter than antimatter? Computational methods for leptogenesis and electroweak baryogenesis*,” *Prog. Part. Nucl. Phys.* **110**, 103727 (2020) [arXiv:1812.02651 [hep-ph]].
- [5] D. Bodeker and W. Buchmuller, “*Baryogenesis from the weak scale to the grand unification scale*,” *Rev. Mod. Phys.* **93**, no.3, 3 (2021) [arXiv:2009.07294 [hep-ph]].
- [6] I. I. Bigi and A. I. Sanda, “*CP Violation*”, ISBN-13: 9780521847940, Second Edition, Cambridge Monographs on Particle Physics, Nuclear Physics, and Cosmology, **28**, 2009.
- [7] A. Ceccucci, Z. Ligeti and Y. Sakai, “*CKM Quark Mixing Matrix*”, (Chapter 12) and T. Gershon and Y. Nir, “*CP Violation in the Quark Sector*”, (Chapter 13) of P. A. Zyla *et al.* [Particle Data Group], “*Review of Particle Physics*,” *PTEP* **2020**, no.8, 083C01 (2020).
- [8] M. C. Gonzalez-Garcia and M. Yokoyam, “*Neutrino Masses, Mixing, and Oscillations*”, (Chapter 14) of P. A. Zyla *et al.* [Particle Data Group], “*Review of Particle Physics*,” *PTEP* **2020**, no.8, 083C01 (2020).
- [9] M. N. Rebelo, “*Leptonic CP Violation and Leptogenesis*,” *Dark Matter in Astroparticle and Particle Physics*, pp. 167-180 (2008) [arXiv:0712.1930 [hep-ph]].
- [10] A. Granelli, K. Moffat and S. T. Petcov, “*Aspects of high scale leptogenesis with low-energy leptonic CP violation*,” *JHEP* **11**, 149 (2021) [arXiv:2107.02079 [hep-ph]].
- [11] M. Fukugita and T. Yanagida, “*Baryogenesis Without Grand Unification*,” *Phys. Lett. B* **174**, 45-47 (1986).
- [12] W. Buchmuller, R. D. Peccei and T. Yanagida, “*Leptogenesis as the origin of matter*,” *Ann. Rev. Nucl. Part. Sci.* **55**, 311-355 (2005) [arXiv:hep-ph/0502169 [hep-ph]].
- [13] S. Davidson, E. Nardi and Y. Nir, “*Leptogenesis*,” *Phys. Rept.* **466**, 105-177 (2008) [arXiv:0802.2962 [hep-ph]].
- [14] S. M. Bilenky, C. Giunti and W. Grimus, “*Phenomenology of neutrino oscillations*,” *Prog. Part. Nucl. Phys.* **43**, 1-86 (1999) [arXiv:hep-ph/9812360 [hep-ph]].
- [15] F. P. An *et al.* [Daya Bay], “*Observation of electron-antineutrino disappearance at Daya Bay*,” *Phys. Rev. Lett.* **108**, 171803 (2012) [arXiv:1203.1669 [hep-ex]].
- [16] J. K. Ahn *et al.* [RENO], “*Observation of Reactor Electron Antineutrino Disappearance in the RENO Experiment*,” *Phys. Rev. Lett.* **108**, 191802 (2012) [arXiv:1204.0626 [hep-ex]].
- [17] B. Pontecorvo, “*Inverse beta processes and nonconservation of lepton charge*,” *Zh. Eksp. Teor. Fiz.* **34**, 247 (1957)
- [18] Z. Maki, M. Nakagawa and S. Sakata, “*Remarks on the unified model of elementary particles*,” *Prog. Theor. Phys.* **28**, 870-880 (1962).
- [19] G. J. Feldman, J. Hartnell and T. Kobayashi, “*Long-baseline neutrino oscillation experiments*,” *Adv. High Energy Phys.* **2013**, 475749 (2013) [arXiv:1210.1778 [hep-ex]].
- [20] K. Abe *et al.* [T2K], “*The T2K Experiment*,” *Nucl. Instrum. Meth. A* **659**, 106-135 (2011) [arXiv:1106.1238 [physics.ins-det]].
- [21] D. S. Ayres *et al.* [NOvA], “*NOvA: Proposal to Build a 30 Kiloton Off-Axis Detector to Study $\nu_\mu \rightarrow \nu_e$ Oscillations in the NuMI Beamline*,” [arXiv:hep-ex/0503053 [hep-ex]].
- [22] K. Abe *et al.* [T2K], “*Constraint on the matter-antimatter symmetry-violating phase in neutrino oscillations*,” *Nature* **580**, no.7803, 339-344 (2020) [erratum: *Nature* **583**, no.7814, E16 (2020)] [arXiv:1910.03887 [hep-ex]].
- [23] M. A. Acero *et al.* [NOvA], “*First Measurement of Neutrino Oscillation Parameters using Neutrinos and Antineutrinos by NOvA*,” *Phys. Rev. Lett.* **123**, no.15, 151803 (2019) [arXiv:1906.04907 [hep-ex]].
- [24] K. Abe *et al.* [T2K], “*Improved constraints on neutrino mixing from the T2K experiment with 3.13×10^{21} protons on target*,” *Phys. Rev. D* **103**, no.11, 112008 (2021) [arXiv:2101.03779 [hep-ex]].
- [25] M. A. Acero *et al.* [NOvA and R. Group], “*An Improved Measurement of Neutrino Oscillation Parameters by the NOvA Experiment*,” [arXiv:2108.08219 [hep-ex]].
- [26] U. Rahaman and S. Raut, “*On the tension between the latest NOvA and T2K data*,” [arXiv:2112.13186 [hep-ph]].
- [27] U. Rahaman, S. Razzaque and S. U. Sankar, “*A review of the tension between the T2K and NOvA appearance data and hints to new physics*,” [arXiv:2201.03250 [hep-ph]].
- [28] L. Wolfenstein, “*Neutrino Oscillations in Matter*,” *Phys. Rev. D* **17** (1978), 2369-2374
- [29] O. G. Miranda and H. Nunokawa, “*Non standard neutrino interactions: current status and future prospects*,” *New J. Phys.* **17**, no.9, 095002 (2015) [arXiv:1505.06254 [hep-ph]].
- [30] Y. Farzan and M. Tortola, “*Neutrino oscillations and Non-Standard Interactions*,” *Front. in Phys.* **6**, 10 (2018) [arXiv:1710.09360 [hep-ph]].
- [31] P. B. Denton, J. Gehrlein and R. Pestes, “*CP -Violating Neutrino Nonstandard Interactions in Long-Baseline-Accelerator Data*,” *Phys. Rev. Lett.* **126**, no.5, 051801 (2021) [arXiv:2008.01110 [hep-ph]].
- [32] S. S. Chatterjee and A. Palazzo, “*Nonstandard Neutrino Interactions as a Solution to the NOvA and T2K Discrepancy*,” *Phys. Rev. Lett.* **126**, no.5, 051802 (2021) [arXiv:2008.04161 [hep-ph]].
- [33] U. Rahaman, “*Looking for Lorentz invariance violation (LIV) in the latest long baseline accelerator neutrino oscillation data*,” *Eur. Phys. J. C* **81**, no.9, 792 (2021) [arXiv:2103.04576 [hep-ph]].
- [34] E. Fernandez-Martinez, M. B. Gavela, J. Lopez-Pavon and O. Yasuda, “*CP-violation from non-unitary leptonic mixing*,” *Phys. Lett. B* **649**, 427-435 (2007) [arXiv:hep-ph/0703098 [hep-ph]].
- [35] S. Antusch, S. Blanchet, M. Blennow and E. Fernandez-Martinez, “*Non-unitary Leptonic Mixing and Leptogenesis*,” *JHEP* **01**, 017 (2010) [arXiv:0910.5957 [hep-ph]].
- [36] I. Martinez-Soler and H. Minakata, “*Standard versus*

- Non-Standard CP Phases in Neutrino Oscillation in Matter with Non-Unitarity*,” *PTEP* **2020**, no.6, 063B01 (2020) [arXiv:1806.10152 [hep-ph]].
- [37] L. S. Miranda, P. Pasquini, U. Rahaman and S. Razzaque, “Searching for non-unitary neutrino oscillations in the present $T2K$ and $NO\nu A$ data,” *Eur. Phys. J. C* **81**, no.5, 444 (2021) [arXiv:1911.09398 [hep-ph]].
- [38] D. V. Forero, C. Giunti, C. A. Ternes and M. Tortola, “Nonunitary neutrino mixing in short and long-baseline experiments,” *Phys. Rev. D* **104**, no.7, 075030 (2021) [arXiv:2103.01998 [hep-ph]].
- [39] S. S. Chatterjee and A. Palazzo, “Interpretation of $NO\nu A$ and $T2K$ data in the presence of a light sterile neutrino,” [arXiv:2005.10338 [hep-ph]].
- [40] S. F. Ge, “Measuring the Leptonic Dirac CP Phase with $TNT2K$,” Contribution to NuPhys2016 [arXiv:1704.08518 [hep-ph]].
- [41] S. F. Ge, “The Leptonic CP Measurement and New Physics Alternatives,” *PoS NuFact2019*, 108 (2020).
- [42] S. F. Ge, “New Physics with Scalar and Dark Non-Standard Interactions in Neutrino Oscillation,” *J. Phys. Conf. Ser.* **1468**, no.1, 012125 (2020).
- [43] K. Abe *et al.* [Hyper-Kamiokande], “Hyper-Kamiokande Design Report,” [arXiv:1805.04163 [physics.ins-det]].
- [44] R. Acciarri *et al.* [DUNE], “Long-Baseline Neutrino Facility (LBNF) and Deep Underground Neutrino Experiment (DUNE): Conceptual Design Report, Volume 2: The Physics Program for DUNE at LBNF,” [arXiv:1512.06148 [physics.ins-det]].
- [45] K. J. Kelly and S. J. Parke, “Matter Density Profile Shape Effects at DUNE,” *Phys. Rev. D* **98** (2018) no.1, 015025 [arXiv:1802.06784 [hep-ph]].
- [46] V. Barger, D. Marfatia and K. Whisnant, “Breaking eight fold degeneracies in neutrino CP violation, mixing, and mass hierarchy,” *Phys. Rev. D* **65** (2002), 073023 [arXiv:hep-ph/0112119 [hep-ph]].
- [47] O. Mena and S. J. Parke, “Untangling CP violation and the mass hierarchy in long baseline experiments,” *Phys. Rev. D* **70** (2004), 093011 [arXiv:hep-ph/0408070 [hep-ph]].
- [48] H. Minakata and H. Nunokawa, “ CP violation versus matter effect in long baseline neutrino oscillation experiments,” *Phys. Rev. D* **57** (1998), 4403-4417 [arXiv:hep-ph/9705208 [hep-ph]].
- [49] C. Boehm *et al.* [Theia], “Theia: Faint objects in motion or the new astrometry frontier,” [arXiv:1707.01348 [astro-ph.IM]].
- [50] V. Fischer [Theia], “Theia: A multi-purpose water-based liquid scintillator detector,” [arXiv:1809.05987 [physics.ins-det]].
- [51] M. Askins *et al.* [Theia], “THEIA: an advanced optical neutrino detector,” *Eur. Phys. J. C* **80**, no.5, 416 (2020) [arXiv:1911.03501 [physics.ins-det]].
- [52] D. Guffanti [THEIA Proto], “Prospects for THEIA: an advanced liquid scintillator neutrino experiment,” *J. Phys. Conf. Ser.* **1468**, no.1, 012124 (2020).
- [53] K. Abe, H. Aihara, A. Ajmi, J. Amey, C. Andreopoulos, M. Antonova, S. Aoki, A. Atherton, S. Ban and F. C. T. Barbato, *et al.* “Proposal for an Extended Run of $T2K$ to 20×10^{21} POT,” [arXiv:1609.04111 [hep-ex]].
- [54] K. Hagiwara, N. Okamura and K. i. Senda, “Solving the neutrino parameter degeneracy by measuring the $T2K$ off-axis beam in Korea,” *Phys. Lett. B* **637**, 266-273 (2006) [erratum: *Phys. Lett. B* **641**, 491 (2006)] [arXiv:hep-ph/0504061 [hep-ph]].
- [55] K. Hagiwara, N. Okamura and K. i. Senda, “Physics potential of $T2KK$: An Extension of the $T2K$ neutrino oscillation experiment with a far detector in Korea,” *Phys. Rev. D* **76**, 093002 (2007) [arXiv:hep-ph/0607255 [hep-ph]].
- [56] K. Abe *et al.* [Hyper-Kamiokande], “Physics potentials with the second Hyper-Kamiokande detector in Korea,” *PTEP* **2018**, no.6, 063C01 (2018) [arXiv:1611.06118 [hep-ex]].
- [57] S. Choubey, M. Ghosh and D. Pramanik, “Sensitivity study of Protvino to ORCA ($P2O$) experiment: effect of antineutrino run, background and systematics,” *Eur. Phys. J. C* **79**, no.7, 603 (2019) [arXiv:1812.02608 [hep-ph]].
- [58] A. Alekou *et al.* [ESSnuSB], “Updated physics performance of the ESSnuSB experiment: ESSnuSB collaboration,” *Eur. Phys. J. C* **81**, no.12, 1130 (2021) [arXiv:2107.07585 [hep-ex]].
- [59] J. Cao, M. He, Z. L. Hou, H. T. Jing, Y. F. Li, Z. H. Li, Y. P. Song, J. Y. Tang, Y. F. Wang and Q. F. Wu, *et al.* “Muon-decay medium-baseline neutrino beam facility,” *Phys. Rev. ST Accel. Beams* **17**, 090101 (2014) [arXiv:1401.8125 [physics.acc-ph]].
- [60] S. Razzaque and A. Y. Smirnov, “Super-PINGU for measurement of the leptonic CP -phase with atmospheric neutrinos,” *JHEP* **05**, 139 (2015) [arXiv:1406.1407 [hep-ph]].
- [61] S. Razzaque and A. Y. Smirnov, “Super-PINGU for measuring CP violation,” *Nucl. Part. Phys. Proc.* **265-266**, 183-185 (2015) [arXiv:1501.03145 [hep-ph]].
- [62] J. Hofestädt, M. Bruchner and T. Eberl, “Super-ORCA: Measuring the leptonic CP -phase with Atmospheric Neutrinos and Beam Neutrinos,” *PoS ICRC2019*, 911 (2020) [arXiv:1907.12983 [hep-ex]].
- [63] F. An *et al.* [JUNO], “Neutrino Physics with JUNO,” *J. Phys. G* **43**, no.3, 030401 (2016) [arXiv:1507.05613 [physics.ins-det]].
- [64] K. J. Kelly, P. A. Machado, I. Martinez Soler, S. J. Parke and Y. F. Perez Gonzalez, “Sub-GeV Atmospheric Neutrinos and CP -Violation in DUNE,” *Phys. Rev. Lett.* **123**, no.8, 081801 (2019) [arXiv:1904.02751 [hep-ph]].
- [65] P. Ballett, S. F. King, S. Pascoli, N. W. Prouse and T. Wang, “Sensitivities and synergies of DUNE and $T2HK$,” *Phys. Rev. D* **96**, no.3, 033003 (2017) [arXiv:1612.07275 [hep-ph]].
- [66] S. K. Raut, “Matter effects at the $T2HK$ and $T2HKK$ experiments,” *Phys. Rev. D* **96**, no.7, 075029 (2017) [arXiv:1703.07136 [hep-ph]].
- [67] K. Chakraborty, K. N. Deepthi and S. Goswami, “Spotlighting the sensitivities of Hyper-Kamiokande, DUNE and ESSnuSB,” *Nucl. Phys. B* **937**, 303-332 (2018) [arXiv:1711.11107 [hep-ph]].
- [68] M. Ghosh and T. Ohlsson, “A comparative study between ESSnuSB and $T2HK$ in determining the leptonic CP phase,” *Mod. Phys. Lett. A* **35**, no.05, 2050058 (2020) [arXiv:1906.05779 [hep-ph]].
- [69] J. Arafune, M. Koike and J. Sato, “ CP violation and matter effect in long baseline neutrino oscillation experiments,” *Phys. Rev. D* **56**, 3093-3099 (1997) [erratum: *Phys. Rev. D* **60**, 119905 (1999)] [arXiv:hep-ph/9703351 [hep-ph]].
- [70] M. Koike and J. Sato, “Effects of matter density fluctuation in long baseline neutrino oscillation experiments,”

- Mod. Phys. Lett. A **14**, 1297-1302 (1999) [arXiv:hep-ph/9803212 [hep-ph]].
- [71] I. Mocioiu and R. Shrock, “Matter effects on neutrino oscillations in long baseline experiments,” *Phys. Rev. D* **62**, 053017 (2000) [arXiv:hep-ph/0002149 [hep-ph]].
- [72] B. Brahmachari, S. Choubey and P. Roy, “CP violation and matter effect for a variable earth density in very long baseline experiments,” *Nucl. Phys. B* **671**, 483-497 (2003) [arXiv:hep-ph/0303078 [hep-ph]].
- [73] S. F. Ge and A. Y. Smirnov, “Non-standard interactions and the CP phase measurements in neutrino oscillations at low energies,” *JHEP* **10**, 138 (2016) [arXiv:1607.08513 [hep-ph]].
- [74] J. Datta, M. Nizam, A. Ajmi and S. U. Sankar, “Matter vs vacuum oscillations in atmospheric neutrinos,” *Nucl. Phys. B* **961** (2020), 115251 [arXiv:1907.08966 [hep-ph]].
- [75] S. P. Mikheyev and A. Y. Smirnov, “Resonance Amplification of Oscillations in Matter and Spectroscopy of Solar Neutrinos,” *Sov. J. Nucl. Phys.* **42** (1985), 913-917.
- [76] M. Freund, “Analytic approximations for three neutrino oscillation parameters and probabilities in matter,” *Phys. Rev. D* **64** (2001), 053003 [arXiv:hep-ph/0103300 [hep-ph]].
- [77] E. K. Akhmedov, R. Johansson, M. Lindner, T. Ohlsson and T. Schwetz, “Series expansions for three flavor neutrino oscillation probabilities in matter,” *JHEP* **04**, 078 (2004) [arXiv:hep-ph/0402175 [hep-ph]].
- [78] P. Coloma, A. Donini, E. Fernandez-Martinez and P. Hernandez, “Precision on leptonic mixing parameters at future neutrino oscillation experiments,” *JHEP* **06**, 073 (2012) [arXiv:1203.5651 [hep-ph]].
- [79] H. J. He and X. J. Xu, “Connecting the leptonic unitarity triangle to neutrino oscillation with CP violation in the vacuum and in matter,” *Phys. Rev. D* **95**, no.3, 033002 (2017) [arXiv:1606.04054 [hep-ph]].
- [80] M. Cho, Y. ChoeJo, H. S. Lee, Y. M. Lee and S. K. Raut, “Neutrino oscillations at dual baselines,” [arXiv:1907.01185 [hep-ph]].
- [81] S. F. King, S. Molina Sedgwick, S. J. Parke and N. W. Prouse, “Effects of matter density profiles on neutrino oscillations for T2HK and T2HKK,” *Phys. Rev. D* **101**, 076019 (2020) [arXiv:2001.05505 [hep-ph]].
- [82] H. Minakata and H. Nunokawa, “Measuring leptonic CP violation by low-energy neutrino oscillation experiments,” *Phys. Lett. B* **495**, 369-377 (2000) [arXiv:hep-ph/0004114 [hep-ph]].
- [83] S. K. Agarwalla, P. Huber, J. M. Link and D. Mohapatra, “A new approach to anti-neutrino running in long baseline neutrino oscillation experiments,” *JHEP* **04**, 099 (2011) [arXiv:1005.4055 [hep-ph]].
- [84] J. Alonso, F. T. Avignone, W. A. Barletta, R. Barlow, H. T. Baumgartner, A. Bernstein, E. Blucher, L. Bugel, L. Calabretta and L. Camilleri, *et al.* “Expression of Interest for a Novel Search for CP Violation in the Neutrino Sector: DAE δ ALUS,” [arXiv:1006.0260 [physics.ins-det]].
- [85] E. Ciuffoli, J. Evslin and X. Zhang, “The Leptonic CP Phase from Muon Decay at Rest with Two Detectors,” *JHEP* **12**, 051 (2014) [arXiv:1401.3977 [hep-ph]].
- [86] M. V. Smirnov, Z. J. Hu, S. J. Li and J. J. Ling, “The possibility of leptonic CP-violation measurement with JUNO,” *Nucl. Phys. B* **931**, 437-445 (2018) [arXiv:1802.03677 [hep-ph]].
- [87] J. Evslin, S. F. Ge and K. Hagiwara, “The leptonic CP phase from T2(H)K and μ^+ decay at rest,” *JHEP* **02**, 137 (2016) [arXiv:1506.05023 [hep-ph]].
- [88] S. F. Ge, P. Pasquini, M. Tortola and J. W. F. Valle, “Measuring the leptonic CP phase in neutrino oscillations with nonunitary mixing,” *Phys. Rev. D* **95**, no.3, 033005 (2017) [arXiv:1605.01670 [hep-ph]].
- [89] S. K. Agarwalla, M. Ghosh and S. K. Raut, “A hybrid setup for fundamental unknowns in neutrino oscillations using T2HK (ν) and μ -DAR ($\bar{\nu}$),” *JHEP* **05**, 115 (2017) [arXiv:1704.06116 [hep-ph]].
- [90] C. Soumya, M. Ghosh, S. K. Raut, N. Sinha and P. Mehta, “Probing muonic charged current nonstandard interactions at decay-at-rest facilities in conjunction with T2HK,” *Phys. Rev. D* **101**, no.5, 055009 (2020) [arXiv:1911.05021 [hep-ph]].
- [91] E. Ciuffoli, J. Evslin and F. Zhao, “Neutrino Physics with Accelerator Driven Subcritical Reactors,” *JHEP* **01**, 004 (2016) [arXiv:1509.03494 [hep-ph]].
- [92] R. Harnik, K. J. Kelly and P. A. N. Machado, “Prospects of Measuring Oscillated Decay-at-Rest Neutrinos at Long Baselines,” *Phys. Rev. D* **101**, no.3, 033008 (2020) [arXiv:1911.05088 [hep-ph]].
- [93] G. D. Orebi Gann [THEIA Interest Group], “Physics Potential of an Advanced Scintillation Detector: Introducing THEIA,” [arXiv:1504.08284 [physics.ins-det]].
- [94] H. Wei, Z. Wang and S. Chen, “Discovery potential for supernova relic neutrinos with slow liquid scintillator detectors,” *Phys. Lett. B* **769**, 255-261 (2017) [arXiv:1607.01671 [physics.ins-det]].
- [95] Z. Guo, M. Yeh, R. Zhang, D. W. Cao, M. Qi, Z. Wang and S. Chen, “Slow Liquid Scintillator Candidates for MeV-scale Neutrino Experiments,” *Astropart. Phys.* **109**, 33-40 (2019) [arXiv:1708.07781 [physics.ins-det]].
- [96] J. Caravaca, B. J. Land, M. Yeh and G. D. Orebi Gann, “Characterization of water-based liquid scintillator for Cherenkov and scintillation separation,” *Eur. Phys. J. C* **80**, no.9, 867 (2020) [arXiv:2006.00173 [physics.ins-det]].
- [97] J. Sawatzki, M. Wurm and D. Kresse, “Detecting the Diffuse Supernova Neutrino Background in the future Water-based Liquid Scintillator Detector Theia,” *Phys. Rev. D* **103**, no.2, 023021 (2021) [arXiv:2007.14705 [physics.ins-det]].
- [98] B. J. Land, Z. Bagdasarian, J. Caravaca, M. Smiley, M. Yeh and G. D. Orebi Gann, “MeV-scale performance of water-based and pure liquid scintillator detectors,” *Phys. Rev. D* **103**, no.5, 052004 (2021) [arXiv:2007.14999 [physics.ins-det]].
- [99] A. Aguilar-Arevalo *et al.* [LSND], “Evidence for neutrino oscillations from the observation of $\bar{\nu}_e$ appearance in a $\bar{\nu}_\mu$ beam,” *Phys. Rev. D* **64**, 112007 (2001) [arXiv:hep-ex/0104049 [hep-ex]].
- [100] S. F. Ge, K. Hagiwara, N. Okamura and Y. Takaesu, “Determination of mass hierarchy with medium baseline reactor neutrino experiments,” *JHEP* **05**, 131 (2013) [arXiv:1210.8141 [hep-ph]].
- [101] C. Andreopoulos, A. Bell, D. Bhattacharya, F. Cavanna, J. Dobson, S. Dytman, H. Gallagher, P. Guzowski, R. Hatcher and P. Kehayias, *et al.* “The GENIE Neutrino Monte Carlo Generator,” *Nucl. Instrum. Meth. A* **614** (2010), 87-104 [arXiv:0905.2517 [hep-ph]].
- [102] C. Andreopoulos, C. Barry, S. Dytman, H. Gallagher,

- T. Golan, R. Hatcher, G. Perdue and J. Yarba, “*The GENIE Neutrino Monte Carlo Generator: Physics and User Manual*,” [arXiv:1510.05494 [hep-ph]].
- [103] Lasserre Thierry, “*Reactor Antineutrino*”, July 18-30, 2011, International Neutrino Summer School, Cartigny
- [104] K. Abe *et al.* [T2K], “*Measurement of neutrino and antineutrino oscillations by the T2K experiment including a new additional sample of ν_e interactions at the far detector*,” *Phys. Rev. D* **96**, no.9, 092006 (2017) [erratum: *Phys. Rev. D* **98**, no.1, 019902 (2018)] [arXiv:1707.01048 [hep-ex]].
- [105] L. Wei, L. Zhan, J. Cao and W. Wang, “*Improving the Energy Resolution of the Reactor Antineutrino Energy Reconstruction with Positron Direction*,” [arXiv:2005.05034 [physics.ins-det]].
- [106] Michael Wurm, “*DSNB detection in Liquid Scintillator*”, March 16, 2018, FroST Workshop, Fermilab
- [107] M. Askins *et al.* [Theia], “*THEIA: an advanced optical neutrino detector*,” *Eur. Phys. J. C* **80**, no.5, 416 (2020) [arXiv:1911.03501 [physics.ins-det]].
- [108] M. Shaevitz [IsoDAR/DAEdALUS], “*Searching for Sterile Neutrinos and CP Violation: The IsoDAR and DAEdALUS Experiments*,” *PoS NEUTEL2015*, 034 (2015)
- [109] T. A. Mueller, D. Lhuillier, M. Fallot, A. Letourneau, S. Cormon, M. Fechner, L. Giot, T. Lasserre, J. Martino and G. Mention, *et al.* “*Improved Predictions of Reactor Antineutrino Spectra*,” *Phys. Rev. C* **83**, 054615 (2011) [arXiv:1101.2663 [hep-ex]].
- [110] P. Huber, “*On the determination of anti-neutrino spectra from nuclear reactors*,” *Phys. Rev. C* **84**, 024617 (2011) [erratum: *Phys. Rev. C* **85**, 029901 (2012)] [arXiv:1106.0687 [hep-ph]].
- [111] J. N. Bahcall and R. K. Ulrich, “*Solar Models, Neutrino Experiments and Helioseismology*,” *Rev. Mod. Phys.* **60**, 297-372 (1988)
- [112] F. Mantovani, L. Carmignani, G. Fiorentini and M. Lissia, “*Anti-neutrinos from the earth: The Reference model and its uncertainties*,” *Phys. Rev. D* **69**, 013001 (2004) [arXiv:hep-ph/0309013 [hep-ph]].
- [113] O. Sramek, W. F. McDonough, E. S. Kite, V. Lekic, S. Dye and S. Zhong, “*Geophysical and geochemical constraints on geoneutrino fluxes from Earth’s mantle*,” *Earth Planet. Sci. Lett.* **361**, 356-366 (2013) [arXiv:1207.0853 [physics.geo-ph]].
- [114] A. S. Dighe and A. Y. Smirnov, “*Identifying the neutrino mass spectrum from the neutrino burst from a supernova*,” *Phys. Rev. D* **62**, 033007 (2000) [arXiv:hep-ph/9907423 [hep-ph]].
- [115] M. T. Keil, G. G. Raffelt and H. T. Janka, “*Monte Carlo study of supernova neutrino spectra formation*,” *Astrophys. J.* **590**, 971-991 (2003) [arXiv:astro-ph/0208035 [astro-ph]].
- [116] P. Vogel and J. F. Beacom, “*Angular distribution of neutron inverse beta decay, $\bar{\nu}_e + p \rightarrow e^+ + n$* ,” *Phys. Rev. D* **60**, 053003 (1999) [arXiv:hep-ph/9903554 [hep-ph]].
- [117] J. A. Formaggio and G. P. Zeller, “*From eV to EeV: Neutrino Cross Sections Across Energy Scales*,” *Rev. Mod. Phys.* **84**, 1307-1341 (2012) [arXiv:1305.7513 [hep-ex]].
- [118] M. Sajjad Athar, M. Honda, T. Kajita, K. Kasahara and S. Midorikawa, “*Atmospheric neutrino flux at INO, South Pole and Pyhasalmi*,” *Phys. Lett. B* **718**, 1375-1380 (2013) [arXiv:1210.5154 [hep-ph]].
- [119] Low energy atmospheric neutrino flux at M.Honda’s website
- [120] M. Sajjad Athar and J. G. Morfín, “*Neutrino(antineutrino)-nucleus interactions in the shallow and deep-inelastic scattering regions*,” *J. Phys. G* **48**, no.3, 034001 (2021) [arXiv:2006.08603 [hep-ph]].
- [121] D. E. Groom and S. R. Klein “*Passage of Particles Through Matter*”, (Chapter 34) of P. A. Zyla *et al.* [Particle Data Group], “*Review of Particle Physics*,” *PTEP* **2020**, no.8, 083C01 (2020).
- [122] B. Abi *et al.* [DUNE], “*Experiment Simulation Configurations Approximating DUNE TDR*,” [arXiv:2103.04797 [hep-ex]].
- [123] M. Jiang *et al.* [Super-Kamiokande], “*Atmospheric Neutrino Oscillation Analysis with Improved Event Reconstruction in Super-Kamiokande IV*,” *PTEP* **2019**, no.5, 053F01 (2019) [arXiv:1901.03230 [hep-ex]].
- [124] K. Hagiwara and N. Okamura, “*Re-evaluation of the T2KK physics potential with simulations including backgrounds*,” *JHEP* **07**, 031 (2009) [arXiv:0901.1517 [hep-ph]].
- [125] S. Tobayama, “*An Analysis of the Oscillation of Atmospheric Neutrinos*,” *PhD Thesis*, British Columbia University, 2016.
- [126] A. Adelmann, J. Alonso, W. A. Barletta, J. M. Conrad, M. H. Shaevitz, J. Spitz, M. Toups and L. A. Winslow, “*Cyclotrons as Drivers for Precision Neutrino Measurements*,” *Adv. High Energy Phys.* **2014**, 347097 (2014) [arXiv:1307.6465 [physics.acc-ph]].
- [127] P. Huber, M. Lindner and W. Winter, “*Simulation of long-baseline neutrino oscillation experiments with GLoBES (General Long Baseline Experiment Simulator)*,” *Comput. Phys. Commun.* **167**, 195 (2005) [arXiv:hep-ph/0407333 [hep-ph]].
- [128] P. Huber, J. Kopp, M. Lindner, M. Rolinec and W. Winter, “*New features in the simulation of neutrino oscillation experiments with GLoBES 3.0: General Long Baseline Experiment Simulator*,” *Comput. Phys. Commun.* **177**, 432-438 (2007) [arXiv:hep-ph/0701187 [hep-ph]].
- [129] S. F. Ge, H. J. He and R. Q. Xiao, Appendix B of “*Probing new physics scales from Higgs and electroweak observables at $e^+ e^-$ Higgs factory*,” *JHEP* **10**, 007 (2016) [arXiv:1603.03385 [hep-ph]].
- [130] S. F. Ge, X. G. He, X. D. Ma and J. Sheng, Appendix of “*Revisiting the Fermionic Dark Matter Absorption on Electron Target*,” [arXiv:2201.11497 [hep-ph]].
- [131] P. F. de Salas, D. V. Forero, S. Gariazzo, P. Martínez-Miravé, O. Mena, C. A. Ternes, M. Tórtola and J. W. F. Valle, “*2020 global reassessment of the neutrino oscillation picture*,” *JHEP* **02** (2021), 071 [arXiv:2006.11237 [hep-ph]]. See tables in Valencia neutrino global fit.
- [132] S. Bharti, U. Rahaman and S. Uma Sankar, “*Matter versus vacuum oscillations at long-baseline accelerator neutrino experiments*,” *Mod. Phys. Lett. A* **36**, no.13, 2150098 (2021) [arXiv:2001.08676 [hep-ph]].
- [133] V. De Romeri, E. Fernandez-Martinez and M. Sorel, “*Neutrino oscillations at DUNE with improved energy reconstruction*,” *JHEP* **09**, 030 (2016) [arXiv:1607.00293 [hep-ph]].
- [134] B. Roe, “*Matter density versus distance for the neutrino beam from Fermilab to Lead, South Dakota, and comparison of oscillations with variable and con-*

- stant density,” *Phys. Rev. D* **95**, no.11, 113004 (2017) [arXiv:1707.02322 [hep-ex]].
- [135] B. Abi *et al.* [DUNE], “Long-baseline neutrino oscillation physics potential of the DUNE experiment,” *Eur. Phys. J. C* **80**, no.10, 978 (2020) [arXiv:2006.16043 [hep-ex]].
- [136] J. Rout, S. Shafaq, M. Bishai and P. Mehta, “Physics prospects with the second oscillation maximum at the Deep Underground Neutrino Experiment,” *Phys. Rev. D* **103**, no.11, 116003 (2021) [arXiv:2012.08269 [hep-ph]].
- [137] S. S. Chatterjee, P. S. B. Dev and P. A. N. Machado, “Impact of improved energy resolution on DUNE sensitivity to neutrino non-standard interactions,” *JHEP* **08**, 163 (2021) [arXiv:2106.04597 [hep-ph]].
- [138] J. Tang, S. Vihonen and T. C. Wang, “Precision measurements on δ_{CP} in MOMENT,” *JHEP* **12**, 130 (2019) [arXiv:1909.01548 [hep-ph]].
- [139] M. Honda, M. Sajjad Athar, T. Kajita, K. Kasahara and S. Midorikawa, “Atmospheric neutrino flux calculation using the NRLMSISE-00 atmospheric model,” *Phys. Rev. D* **92**, no.2, 023004 (2015) [arXiv:1502.03916 [astro-ph.HE]].
- [140] A. M. Dziewonski and D. L. Anderson, “Preliminary reference earth model,” *Phys. Earth Planet. Interiors* **25**, 297-356 (1981)